

**STUDY OF FOURIER TRANSFORM PROFILOMETRY  
BY USING BACKGROUND ELIMINATION**

**Jaroon Wongjarern**



**A Thesis Submitted in Partial Fulfillment of the Requirements for  
the Degree of Master of Science in Laser Technology**

**Suranaree University of Technology**

**Academic Year 2015**

# การศึกษาการแปลงฟูรีเยร์โพรไฟล์โคมทรีโดยใช้การกำจัดพื้นหลัง



วิทยานิพนธ์นี้เป็นส่วนหนึ่งของการศึกษาตามหลักสูตรปริญญาวิทยาศาสตรมหาบัณฑิต

สาขาวิชาเทคโนโลยีเลเซอร์

มหาวิทยาลัยเทคโนโลยีสุรนารี

ปีการศึกษา 2558

**STUDY OF FOURIER TRANSFORM PROFILOMETRY  
BY USING BACKGROUND ELIMINATION**

Suranaree University of Technology has approved this thesis submitted in partial fulfillment of the requirements for a Master's Degree.

Thesis Examining Committee

---

(Prof. Dr. Santi Maensiri)

Chairperson

---

(Prof. Dr. Joewono Widjaja)

Member (Thesis Advisor)

---

(Dr. Panomsak Meemon)

Member

---

(Dr. Boonsong Sutapun)

Member

---

(Prof. Dr. Sukit Limpijumnong)

Vice Rector for Academic Affairs  
and Innovation

---

(Prof. Dr. Santi Maensiri)

Dean of Institute of Science

จรรยา วงษ์เจริญ : การศึกษาการแปลงฟูรีเยร์โปรไฟล์โลเมทรีโดยใช้การกำจัดพื้นหลัง  
(STUDY OF FOURIER TRANSFORM PROFILOMETRY BY USING  
BACKGROUND ELIMINATION) อาจารย์ที่ปรึกษา : ศาสตราจารย์ ดร.ยูวโน  
วิจิตยา, 65 หน้า.

งานวิทยานิพนธ์นี้นำเสนอการศึกษาวิธีใหม่สำหรับการขจัดสัญญาณพื้นหลังที่ไม่พึงประสงค์ในการแปลงฟูรีเยร์โปรไฟล์โลเมทรีโดยการใช้ภาพวัตถุและภาพระนาบอ้างอิง สำหรับวิธีการดำเนินการของวิธีที่นำเสนอนี้ ค่าความเข้มเฉลี่ยของในแต่ละภาพจะถูกลบออกเป็นลำดับแรก ส่วนประการที่สอง ผลลัพธ์ของค่าความเข้มของภาพวัตถุและภาพระนาบอ้างอิงที่ถูกหักออกจะมีค่าแตกต่างกันซึ่งได้ถูกหักออกจากภาพเกรตติงที่ผิดรูป ทั้งหมดนี้จะช่วยลดทอนสัญญาณพื้นหลังที่ไม่สม่ำเสมอได้ หลังจากการแปลงฟูรีเยร์ ข้อมูลเฟสสามารถสกัดได้จากคลื่นความถี่พื้นฐานและได้ถูกนำมาใช้เพื่อสร้างความสูงของวัตถุ ผลการทดลองทำการตรวจสอบได้ว่า แม้ว่าวิธีการที่นำเสนอนี้จำนวนของรูปแบบเกรตติงที่ถูกใช้จะเท่ากับกับวิธีการแปลงฟูรีเยร์โปรไฟล์โลเมทรีแบบดั้งเดิม แต่ทว่าประสิทธิภาพของการตรวจวัดสำหรับวิธีที่นำเสนอที่ดีเหมือนกับวิธีการแปลงฟูรีเยร์ด้วยการขยับเฟส ดังนั้น วิธีการที่นำเสนอนี้ ความผิดพลาดของเฟสที่เกิดจากความไม่แน่นอนของเกรตติงจะลดน้อยลง

JAROON WONGJARERN : STUDY OF FOURIER TRANSFORM  
PROFILOMETRY BY USING BACKGROUND ELIMINATION.

THESIS ADVISOR : PROF. JOEWONO WIDJAJA, Ph.D. 65 PP.

FOURIER TRANSFORM PROFILOMETRY/BACKGROUND ELIMINATION/3D  
SHAPE MEASUREMENT/CONTRAST RATIO/GRATING PROJECTION

A new method for eliminating an unwanted background signal in Fourier transform profilometry by using images of an object and a reference plane is proposed. To implement the proposed method, a mean intensity value of each image is firstly removed. Secondly, the resultant images of the object and the reference plane scaled by their contrasts are subtracted from their corresponding deformed grating images. This removes totally the non-uniform background signal. After taking its Fourier transform, a phase information can be extracted from a fundamental spectrum and is used to reconstruct the object height. The experimental results verify that although the proposed method employs the same number of grating patterns as the conventional Fourier transform profilometry, its measurement performance is as good as that of the  $\pi$ -phase shifting method. Therefore, the proposed method suffers less from a phase error caused by a grating jitter.

School of Physics

Academic Year 2015

Student's Signature \_\_\_\_\_

Advisor's Signature \_\_\_\_\_

## **ACKNOWLEDGEMENTS**

First of all, I would like to express my sincere thanks to my thesis advisor, Prof. Dr. Joewono Widjaja for his invaluable help and constant encouragement throughout the course of this research. I am most grateful for his teaching and advice, not only on research methodology but also philosophy of life. I would not have achieved this far and this thesis would not have been completed without all the support that I have always received from him.

In addition, I am grateful for to all faculties of Laser Technology Program, School of Physics: Prof. Dr. Santi Maensiri, Dr. Sukanya Tatchatraiphop, Dr. Panomsak Meemon, and all students for suggestions and help. I would also like to thank Suranaree University of Technology and Institute of Research and development for a thesis support grant, respectively.

Finally, I most gratefully acknowledge my parents and my friends for all their support throughout the period of this research.

Jaroon Wongjarern

# CONTENTS

	<b>Page</b>
ABSTRACT IN THAI.....	I
ABSTRACT IN ENGLISH .....	II
ACKNOWLEDGEMENTS .....	III
CONTENTS.....	IV
LIST OF TABLES .....	VI
LIST OF FIGURES .....	VII
<b>CHAPTER</b>	
<b>I INTRODUCTION.....</b>	<b>1</b>
1.1 Background .....	1
1.2 Significance of the Study .....	3
1.3 Research Objectives.....	4
1.4 Scope and Limitation of the Study.....	4
1.5 Organization of the Thesis .....	4
<b>II FOURIER TRANSFORM PROFILOMETRY.....</b>	<b>6</b>
2.1 Conventional FTP .....	6
2.2 FTP Using $\pi$ -Phase Shifting Method .....	15
<b>III BACKGROUND ELIMINATION METHOD .....</b>	<b>19</b>
3.1 Introduction.....	19
3.2 FTP Using Background Elimination Method .....	20

## CONTENTS (Continued)

	<b>Page</b>
<b>IV EXPERIMENTAL VERIFICATIONS</b> .....	26
4.1 Experimental Setup .....	26
4.2 Calibration of the Distances $l_0$ and $d$ .....	29
4.3 Algorithm of the Proposed FTP Method .....	30
4.4 Results and Discussions .....	31
4.4.1 Isosceles Prism Object with Low Slope .....	31
4.4.2 Isosceles Prism Object with High Slope .....	40
4.4.3 Arbitrary-Shaped Bottle .....	48
<b>V CONCLUSIONS</b> .....	59
5.1 Conclusions .....	59
5.2 Future Work .....	60
REFERENCES .....	61
CURRICULUM VITAE .....	65

## LIST OF TABLES

Table	Page
4.1	The grating pitch $p_0$ of the proposed FTP as a function of the angle $\theta$ ..... 28
4.2	The distance $d$ and the maximum measurable slope of the proposed FTP ... 29



## LIST OF FIGURES

<b>Figure</b>	<b>Page</b>
1	A schematic setup for implementing 3-D shape measurement by using the FTP method..... 2
2.1	A schematic diagram of an optical setup for implementing the FTP ..... 6
2.2	Images of the grating pattern deformed by (a) the isosceles prism and (b) the reference plane..... 7
2.3	Power spectra of (a) a 1-D signal pattern scanned at the 100 <sup>th</sup> row of the grating image shown in Figure 2.2(a) and (b) its filtered +1 <sup>st</sup> order $C(f_x - f_0, 100)$ ..... 9
2.4	Power spectra of (a) a 1-D signal pattern scanned at the 100 <sup>th</sup> row of the grating image shown in Figure 2.2(b) and (b) its filtered +1 <sup>st</sup> order $C(f_x - f_0, 100)$ ..... 10
2.5	Power spectra of the 0 <sup>th</sup> and the +1 <sup>st</sup> order power spectra of the deformed Ronchi grating ..... 11
2.6	Incorrect reconstruction of the isosceles prism by the conventional FTP ..... 13
2.7	Profile of the isosceles prism ..... 14
2.8	Power spectra of the grating deformed by the isosceles prism..... 14
2.9	Intensities scanned at the row 100 <sup>th</sup> of the grating images deformed by (a) the object and (b) the object with the $\pi$ -phase shifting method,

## LIST OF FIGURES (Continued)

Figure	Page
(c) the reference plane and (d) the reference plane with the $\pi$ -phase shifting method .....	16
2.10 Power spectra of a 1-D signal pattern scanned at the 100 <sup>th</sup> row of the grating deformed by (a) the object and (b) the reference plane obtained by using $\pi$ -phase shifting method. The filtered +1 <sup>st</sup> order spectra $C(f_x - f_0, 100)$ of (c) Figure (a) and (d) Figure (b).....	17
3.1 Images of (a) the isosceles prism and (b) the flat reference plane obtained by using the uniform light illumination .....	20
3.2 Intensities scanned at the 100 <sup>th</sup> row of the grating images deformed by (a) the object and (b) the reference plane. Intensities scanned at the 100 <sup>th</sup> row of the images of (c) the object and (d) the reference plane.....	22
3.3 Intensities scanned at the 100 <sup>th</sup> row of (a) $g_1(x, 100) - g_{1dc}$ , (b) $g_2(x, 100) - g_{2dc}$ , (c) $[g_3(x, 100) - g_{3dc}] / c_r'$ , (d) $[g_4(x, 100) - g_{4dc}] / c_r''$ , (e) Eq. (3.4) and (f) Eq. (3.5) .....	23
3.4 Power spectra of the grating pattern deformed by (a) the object and (b) the reference plane which are obtained by eliminating the unwanted background. The filtered +1 <sup>st</sup> order spectra $C(f_x - f_0, 100)$ of (c) Figure (a) and (d) Figure (b) .....	24
4.1 Optical setup for implementing the FTP.....	27

## LIST OF FIGURES (Continued)

Figure	Page
4.2	Two isosceles prism with the heights of (a) 42.71 mm, (b) 81.24 mm and (c) a 600 ml plastic water bottle..... 28
4.3	A block diagram of a numerical calculation for the surface reconstruction by using the background elimination method ..... 30
4.4	Images of the grating pattern deformed by the isosceles prism with the slope 0.64 in situation that the projected gratings have the pitch of (a) 4.84 mm and (b) 3.24 mm at the angle $\theta = 4^\circ$ . Intensities scanned at the 100 <sup>th</sup> row of (c) Figure (a) and (d) Figure (b)..... 31
4.5	Images of the grating pattern deformed by the isosceles prism object with the slope 0.64 in situation that the projected gratings have the pitch of (a) 4.84 mm and (b) 3.24 mm at the angle $\theta = 28^\circ$ . Intensities scanned at the 100 <sup>th</sup> row of (c) Figure (a) and (d) Figure (b)..... 33
4.6	Intensities scanned at the 100 <sup>th</sup> row of the background eliminated grating patterns obtained from (a) Figure 4.4(a), (b) Figure 4.4(b), (c) Figure 4.5(a) and (d) Figure 4.5(b)..... 34
4.7	Power spectra of the background eliminated grating patterns obtained from (a) Figure 4.6(a), (b) Figure 4.6(b), (c) Figure 4.6(c) and (d) Figure 4.6(d) ..... 35
4.8	Height profiles of the isosceles prism with the slope of 0.64 reconstructed at the angle $\theta = 4^\circ$ by using the conventional,

## LIST OF FIGURES (Continued)

Figure	Page
<p>the <math>\pi</math>-phase shifting and the proposed FTPs compared with the digital height gauge in situation that the gratings have the pitch of (a) 4.84 mm and (b) 3.24 mm .....</p>	36
<p>4.9 Height profiles of the isosceles prism with the slope of 0.64 reconstructed at the angle <math>\theta = 28^\circ</math> by using the conventional, the <math>\pi</math>-phase shifting and the proposed FTPs compared with the digital height gauge in situation that the gratings have the pitch of (a) 4.84 mm and (b) 3.24 mm.....</p>	38
<p>4.10 3-D height profile of the isosceles prism reconstructed in situation that the projected grating has the pitch of 4.84 mm at the angle <math>\theta = 28^\circ</math> by using (a) the <math>\pi</math>-phase shifting and (b) the proposed methods.....</p>	39
<p>4.11 Images of the grating pattern deformed by the isosceles prism with the slope 1.22 in situation that the projected gratings have the pitch of (a) 4.84 mm and (b) 3.24 mm at the angle <math>\theta = 4^\circ</math> . Intensities scanned at the 100<sup>th</sup> row of (c) Figure (a) and (d) Figure (b).....</p>	40
<p>4.12 Images of the grating pattern deformed by the isosceles prism with the slope 1.22 in situation that the projected gratings have the pitch of (a) 4.84 mm and (b) 3.24 mm at the angle <math>\theta = 28^\circ</math> . Intensities scanned at the 100<sup>th</sup> row of (c) Figure (a) and (d) Figure (b).....</p>	41
<p>4.13 Intensities scanned at the 100<sup>th</sup> row of the background eliminated</p>	

**LIST OF FIGURES (Continued)**

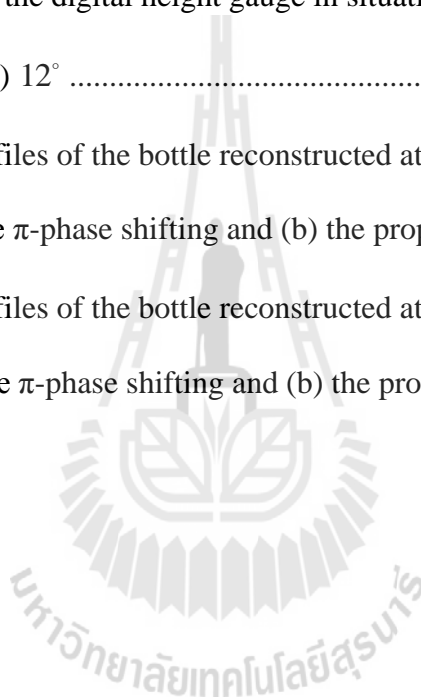
<b>Figure</b>	<b>Page</b>
grating patterns obtained from (a) Figure 4.11(a), (b) Figure 4.11(b), (c) Figure 4.12(a) and (d) Figure 4.12(b).....	42
4.14 Power spectra of the background eliminated grating patterns obtained from (a) Figure 4.13(a), (b) Figure 4.13(b), (c) Figure 4.13(c) and (d) Figure 13(d) .....	43
4.15 Height profiles of the isosceles prism with the slope of 1.22 reconstructed at the angle $\theta = 4^\circ$ by using the conventional, the $\pi$ -phase shifting and the proposed FTPs compared with the digital height gauge in situation that the gratings have the pitch of (a) 4.84 mm and (b) 3.24 mm.....	45
4.16 Height profiles of the isosceles prism with the slope of 1.22 reconstructed at the angle $\theta = 28^\circ$ by using the conventional, the $\pi$ -phase shifting and the proposed FTPs compared with the digital height gauge in situation that the gratings have the pitch of (a) 4.84 mm and (b) 3.24 mm.....	46
4.17 3-D height profile of the isosceles prism reconstructed in situation that the projected grating has the pitch of 4.84 mm at the angle $\theta = 28^\circ$ by using (a) the $\pi$ -phase shifting and (b) the proposed methods .....	47
4.18 Images of the grating patterns deformed by the plastic water	

## LIST OF FIGURES (Continued)

Figure	Page
bottle object in situation that the projected grating has the pitch of 3.24 mm at the angle $\theta$ of (a) $8^\circ$ and (b) $12^\circ$ .....	48
4.19 Intensities scanned at the 131 <sup>th</sup> row of (a) Figure 4.18(a) and (b) Figure 4.18(b). Intensities scanned at the 270 <sup>th</sup> row of (c) Figure 4.18(a) and (d) Figure 4.18(b) .....	49
4.20 Intensities scanned at the 131 <sup>th</sup> row of the background eliminated grating patterns obtained from (a) Figure 4.19(a), (b) Figure 4.19(b). Intensities scanned at the 270 <sup>th</sup> row of the background eliminated grating patterns obtained from (c) Figure 4.19(c) and (d) Figure 4.19(d) .....	50
4.21 Power spectra of the background eliminated grating patterns obtained from (a) Figure 4.20 (a), (b) Figure 4.20(b), (c) Figure 4.20(c), (d) Figure 4.20(d), (e) Figure 4.20(e) and (f) Figure 4.20(f) .....	51
4.22 Height profiles of neck support ring reconstructed by using the conventional, the $\pi$ -phase shifting and the proposed FTPs compared with the digital height gauge in situation that the angle $\theta$ is (a) $8^\circ$ and (b) $12^\circ$ .....	53
4.23 Height profiles of the bottle shoulder reconstructed by using the conventional, the $\pi$ -phase shifting and the proposed FTPs compared with the digital height gauge in situation that the angle $\theta$ is (a) $8^\circ$ and (b) $12^\circ$ .....	54

## LIST OF FIGURES (Continued)

<b>Figure</b>	<b>Page</b>
4.24 Height profiles along the vertical direction of the bottle reconstructed using the conventional, the $\pi$ -phase shifting and the proposed FTPs compared with the digital height gauge in situation that the angle $\theta$ is (a) $8^\circ$ and (b) $12^\circ$ .....	55
4.25 3-D height profiles of the bottle reconstructed at the angle $\theta = 8^\circ$ by using (a) the $\pi$ -phase shifting and (b) the proposed method .....	57
4.26 3-D height profiles of the bottle reconstructed at the angle $\theta = 12^\circ$ By using (a) the $\pi$ -phase shifting and (b) the proposed method .....	58



# CHAPTER I

## INTRODUCTION

### 1.1 Background

The FTP is one of the useful three-dimensional (3-D) shape measurement methods (Takeda and Mutoh, 1983). This is because the FTP can perform full field measurement by using simple white light source. The FTP has been widely used for 3-D noncontact profilometry such as measurement of vibration in drumhead (Zhang and Su, 2005), surface reconstruction of small object and ancient artwork (Quan, He, Wang, Tay, and Shang, 2001; Spagnolo *et al.*, 2000), inspection and profiling of moving objects in machine vision systems (Sajan, Tay, Shang, and Asundi, 1997; Tay, Toh, and Shang, 1998), pre-plastic surgery planning and post-surgery treatment (Su and Chen, 2004; Geng, 2011), input peripherals for computer graphic animations (Gorthi and Rastogi, 2010), retrieve topographic maps of cuticles isolated from the abaxial surface of leaves (Martinez *et al.*, 2012), human face recognition (Gorthi and Rastogi, 2010) and human foot arch deformation under a static load (Meneses, Gharbi, and Cornu, 2002).

Figure 1 show a schematic setup for implementing 3-D shape measurement by using the FTP method. In the FTP, a Ronchi grating or a sinusoidal grating pattern is projected onto an object surface being studied (Su, Zhou, Bally, and Vukicevic, 1992; Zhou and Su, 1994). Due to elevation or depression of the object profile, the projected grating pattern is deformed, modulating its spatial phase. By recording the deformed

pattern by a charge-coupled device (CCD) image sensor and extracting its phase via a Fourier transformation, the 3-D surface profile can be measured. Since the modulated phase is encoded into the fundamental frequency spectra of the grating image, it is necessary to prevent these spectra from being overlapped by the other spectra. This is the inherent drawback of the conventional FTP.

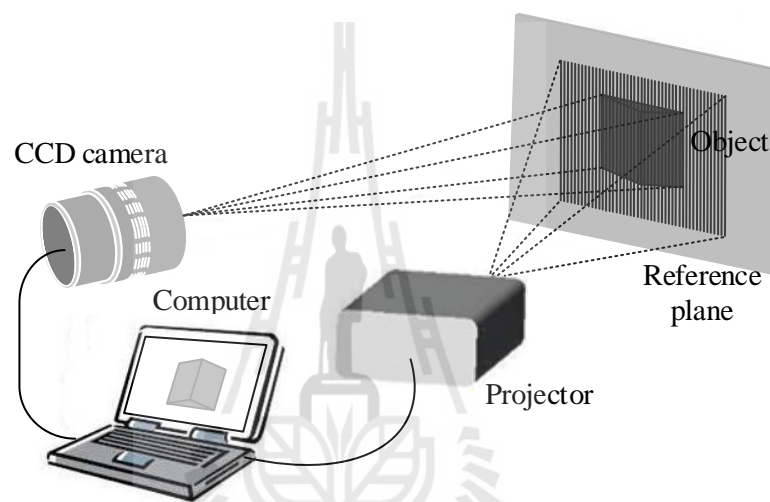


**Figure 1** A schematic setup for implementing 3-D shape measurement by using the FTP method.

In the past decades, several methods for solving this drawback have been reported. Su and Li *et al.* employed a  $\pi$ -phase shifting of a defocused Ronchi grating to improve performance of the FTP (Su and Zhou, 1992; Li, Su, and Guo, 1990). The defocused grating is used to remove higher order frequency spectra, while the  $\pi$ -phase shifting method eliminates the zeroth order spectrum of the background. However, this method suffers from a phase shift error which may arise from imperfect defocusing process. To solve this problem, the  $\pi$ -phase shifting method has been

modified (Yi and Huang, 1997). In this modified FTP, the  $\pi$ -phase shifting grating images deformed by the object and the reference plane are subtracted from the ones recorded without the  $\pi$ -phase shift. When the unwanted background can be removed, the modified method has better accuracy and measurement range.

Later, Tavares *et al.* reported a new method for the background elimination by projecting subsequently two orthogonal sinusoidal gratings generated from a video projector onto the object under test (Tavares and Vaz, 2006). Since the background is eliminated by subtracting two spectra calculated from the two gratings, the resultant spectra consist of four fundamental frequencies. To extract the desired phase from one of the fundamental frequencies, the unwanted fundamental frequencies are removed by applying a zero threshold to the resultant spectra. As a result, negative amplitude of the desired fundamental frequencies may be corrupted.

## 1.2 Significance of the Study

In this study, a new method for improving performance of the FTP by using a background elimination is studied. Instead of using the  $\pi$ -phase shifting grating patterns, the proposed method employs images of the object and the reference plane generated by using uniform light to remove the unwanted background. The reasons for this interest is that firstly, phase of the projected grating pattern may deviate, because of jitter on a LCD projector. This jitter is abrupt variations in amplitude or timing of synchronization signals that cause instability of video or image reproduction (Fukaishi *et al.*, 2000; Hsiao and Lee, 2008; Yamaguchi *et al.*, 2009; Pavlovych and Stuerzlinger, 2010). It may arise from electromagnetic interference, cross talk with carriers of other signals, intrinsic circuit problems, and cable and/or connection issues.

Therefore, the jitter-induced phase error can be obviated by minimizing the number of the projected grating patterns. Secondly, due to less number of the grating patterns, response time to display the patterns is reduced. Therefore, it may be suitable for dynamic measurements.

### **1.3 Research Objectives**

The objectives of this research are two folds. The first objective is to develop a new digital method for the background elimination of the FTP. The second one is to verify feasibility of the proposed FTP by using background elimination method.

### **1.4 Scope and Limitation of the Study**

- 1.4.1 To verify the measureable rate of change of the 3-D surface profile of isosceles prisms with dimensions of  $133.51 \text{ mm} \times 70.1 \text{ mm} \times 42.71 \text{ mm}$  and  $133.12 \text{ mm} \times 70.1 \text{ mm} \times 81.24 \text{ mm}$  and a 600 ml plastic water bottle.
- 1.4.2 The proposed method is experimentally verified.
- 1.4.3 Three-dimensional shape reconstructions obtained by the proposed method are compared with those by the conventional and the  $\pi$ -phase shifting FTPs and a direct contact using a digital height gauge.

### **1.5 Organization of the Thesis**

The remainder of this thesis is organized as follows. In Chapter II, principles of the FTP is firstly reviewed and its drawback is identified. An improvement of the

FTP by using the  $\pi$ -phase shifting method is then discussed. Chapter III discusses the proposed background elimination method which can eliminate the unwanted zeroth-order spectrum of the grating patterns. In Chapter IV, experimental verifications of the proposed method by using the isosceles prism and a complex-shaped objects are presented. The experimental results of the proposed method are compared with those by the conventional FTP and the  $\pi$ -phase shifting method. Finally, conclusions of this research work and suggestion for future research are presented in Chapter V.



## CHAPTER II

### FOURIER TRANSFORM PROFILOMETRY

In this chapter, the theory of the conventional FTP is firstly reviewed. The discussion is started with the principle of measurement of 3-D object shapes proposed by Takeda and Mutoh (1983) including its limitation in measuring objects with high slope. This is followed by a discussion of the  $\pi$ -phase shifting method which is used to improve the measurement performance of the conventional FTP.

#### 2.1 Conventional FTP

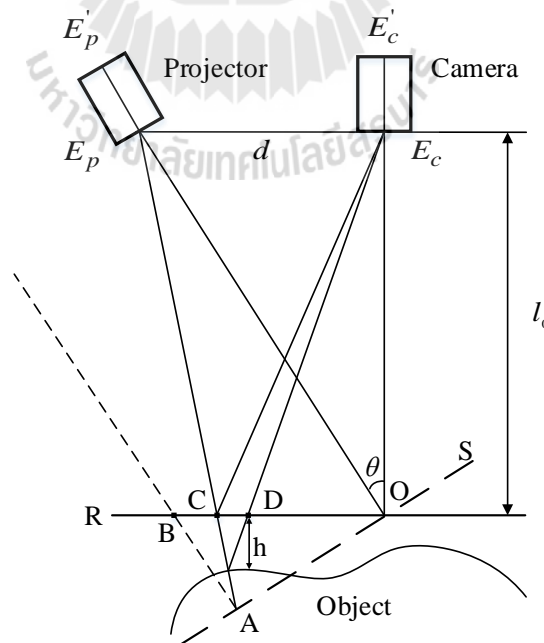


**Figure 2.1** A schematic diagram of an optical setup for implementing the FTP

(Takeda and Mutoh, 1983).

Figure 2.1 shows a schematic diagram of an optical setup for implementing the FTP which consists of a projector and camera systems. Their optical axes lie in the same plane and intersect at the point  $O$  in the reference plane  $R$  from which the height of the object surface is measured.  $E_p$  and  $E'_p$  denote the centers of the entrance and the exit pupils of the projector lens, whereas  $E_c$  and  $E'_c$  are those for the camera. The camera and the projector entrance pupils are at the same distance  $l_0$  from the reference plane, while their spatial separation is  $d$ . Due to this geometry, the two axes make an angle  $\theta$  which is defined as  $\arctan(d/l_0)$ .

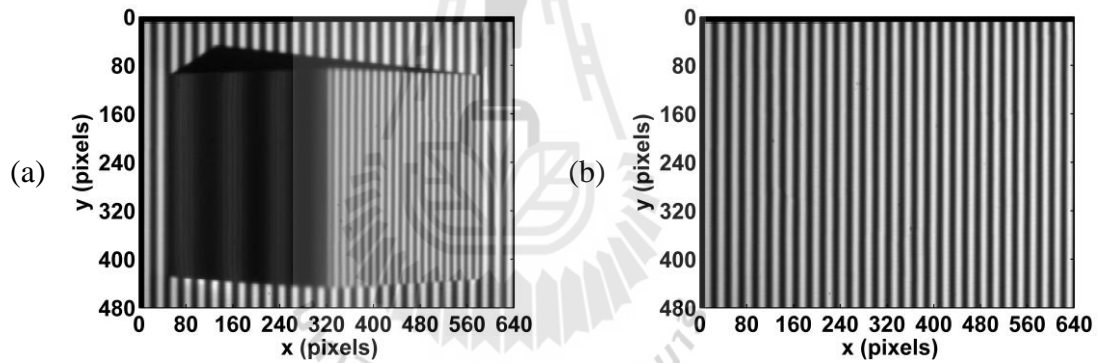


**Figure 2.2** Images of the grating pattern deformed by (a) the isosceles prism and (b) the reference plane, respectively.

Let us consider the 3-D height reconstruction of an isosceles prism by this FTP system. When a sinusoidal grating pattern is projected onto this object prism being measured, its deformed grating pattern shown in Figure 2.2(a) can be expressed as

$$g_1(x, y) = g_{1dc} + o(x, y) + bo(x, y) \cos[2\pi f_0 x + \varphi(x, y)], \quad (2.1)$$

where  $g_{1dc}$  is the dc bias of the recorded image, while  $o(x, y)$  is the irradiance caused by non-uniform light reflection of the object.  $b$  is the modulation factor and  $f_0$  is the fundamental frequency of the observed grating given by

$$f_0 = \frac{1}{p_0} = \frac{\cos\theta}{p}, \quad (2.2)$$

with  $p$  is the grating pitch at the plane  $S$  which is normal to the projector axis.  $\varphi(x, y)$  is the phase modulation caused by the surface height distribution. The phase modulation depends on the height such that the higher object surface gives broader phase modulation. For the sake of simplicity, Eq. (2.1) can be rewritten as

$$g_1(x, y) = g_{1dc} + o(x, y) + c(x, y)\exp(i2\pi f_0 x) + c^*(x, y)\exp(-i2\pi f_0 x) \quad (2.3)$$

with

$$c(x, y) = 0.5bo(x, y)\exp[i\varphi(x, y)]. \quad (2.4)$$

A 1-D Fourier transformation of Eq. (2.3) with respect to the  $x$  direction gives

$$G_1(f_x, y) = g_{1dc}\delta(f_x) + O(f_x, y) + C(f_x - f_0, y) + C^*(f_x + f_0, y), \quad (2.5)$$

where the first, the second, the third and the fourth terms of Eq. (2.5) are the 1-D Fourier spectra of the dc bias,  $o(x, y)$ ,  $c(x, y)$  and  $c^*(x, y)$ , respectively. Figure 2.3(a) shows the spectrum  $G_1(f_x, y)$  of Eq. (2.5). The first two terms which occur at the origin are known as the  $0^{th}$  order spectrum, while the third and the fourth terms correspond to the  $+1^{st}$  and the  $-1^{st}$  orders of the frequency spectra, respectively. They are separated from the  $0^{th}$  order spectrum by the fundamental frequency  $f_0$ . According to Eq. (2.5), the desired phase modulation is encoded as the width of the  $+1^{st}$  and the  $-1^{st}$  fundamental frequency spectra. Therefore, the 3-D shape can be accurately measured, provided the fundamental frequency spectral information is not

corrupted by the overlapping of the  $0^{th}$  order spectrum. When there is no spectral overlapping, the filtering of one fundamental spectrum such as  $C(f_x - f_0, 100)$  shown in Figure 2.3(b) and taking its inverse Fourier transform gives a complex signal

$$g_1'(x, y) = 0.5bo(x, y)\exp\{i[2\pi f_0 x + \varphi(x, y)]\}. \quad (2.6)$$

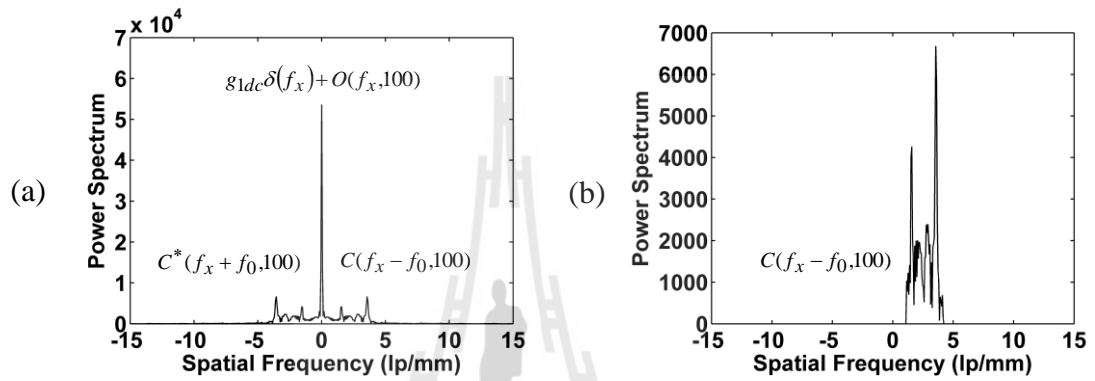


**Figure 2.3** Power spectra of (a) a 1-D signal pattern scanned at the  $100^{th}$  row of the grating image shown in Figures 2.2(a) and (b) its filtered +1<sup>st</sup> order  $C(f_x - f_0, 100)$ , respectively.

In order to have a zero reference height, a second grating image deformed by a flat and uniform reference plane as shown in Figure 2.2(b)

$$g_2(x, y) = g_{2dc} + r(x, y) + br(x, y)\cos[2\pi f_0 x + \varphi_0(x, y)] \quad (2.7)$$

is recorded. Here,  $r(x, y)$  corresponds of the irradiance caused by non-uniform light reflection of the reference plane, while  $\varphi_0(x, y)$  is the phase distribution corresponding to the zero height. By applying the same filtering to its fundamental spectrum shown in Figure 2.4(b), a complex signal

$$g_2'(x, y) = 0.5br(x, y)\exp\{i[2\pi f_0 x + \varphi_0(x, y)]\} \quad (2.8)$$

is generated. The product of Eq. (2.6) and a complex conjugate of Eq. (2.8) gives

$$g_1'(x, y) \cdot g_2^*(x, y) = 0.25b^2 o(x, y)r(x, y)\exp\{i[\varphi(x, y) - \varphi_0(x, y)]\}. \quad (2.9)$$

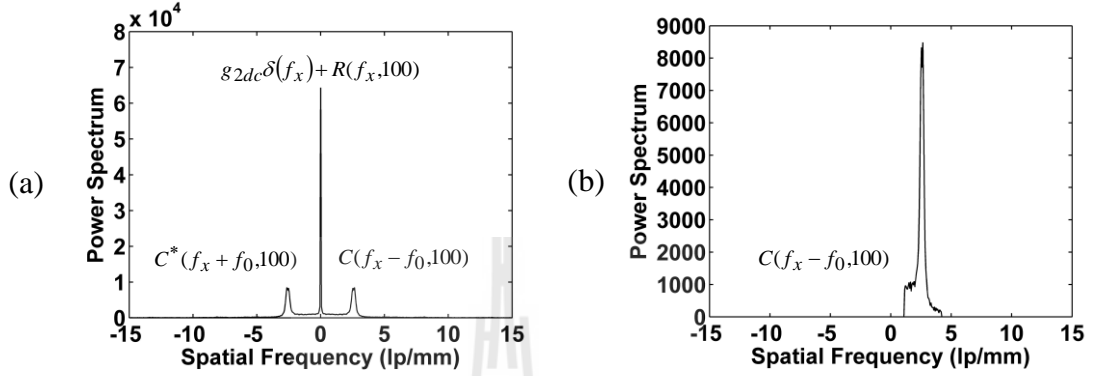


**Figure 2.4** Power spectra of (a) a 1-D signal pattern scanned at the 100<sup>th</sup> row of the grating image shown in Figure 2.2(b) and (b) its filtered +1<sup>st</sup> order  $C(f_x - f_0, 100)$ , respectively.

The phase modulation due to the object height distribution can be extracted by calculating a complex logarithm of Eq. (2.9)

$$\log[g_1'(x, y) \cdot g_2^*(x, y)] = \log[0.25b^2 o(x, y)r(x, y)] + i[\varphi(x, y) - \varphi_0(x, y)]. \quad (2.10)$$

The phase difference  $\varphi(x, y) - \varphi_0(x, y)$  in the imaginary part is completely separated from the unwanted amplitude variation  $b^2 o(x, y)r(x, y)$  in the real part. The phase difference is related to the desired height (Takeda and Mutoh, 1983)

$$h(x, y) = \frac{l_0[\varphi(x, y) - \varphi_0(x, y)]}{[\varphi(x, y) - \varphi_0(x, y)] - 2\pi f_0 d}. \quad (2.11)$$

By substituting the phase difference  $\varphi(x, y) - \varphi_0(x, y)$  into Eq. (2.11), the object profile  $h(x, y)$  is obtained.

According to the frequency modulation theory, an instantaneous frequency of the  $n^{\text{th}}$  spectrum component of frequency-modulated signals can be written as

$$f_n = nf_0 \pm \frac{n}{2\pi} \frac{\partial \phi(x, y)}{\partial x}. \quad (2.12)$$

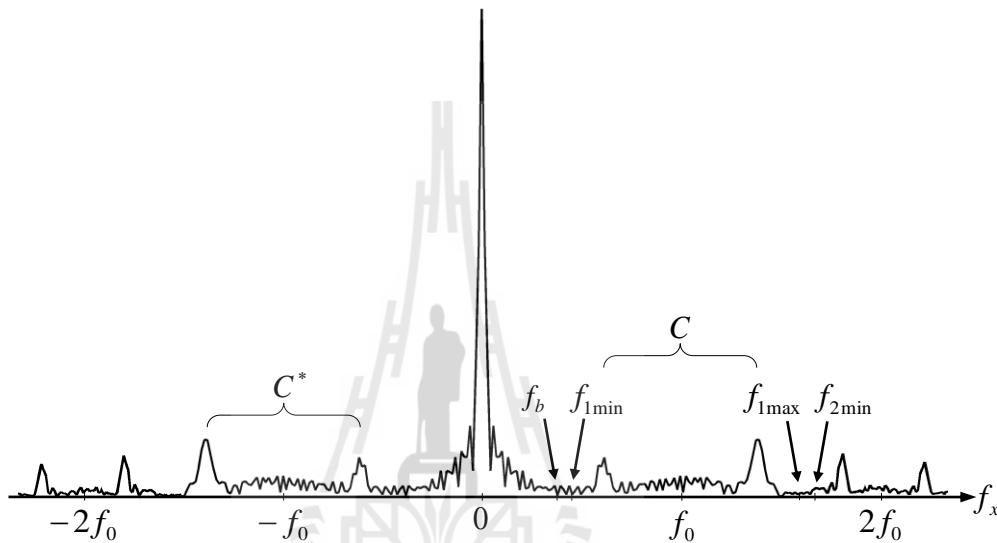


**Figure 2.5** Power spectra of the  $0^{\text{th}}$  and the  $+1^{\text{st}}$  order power spectra of the deformed Ronchi grating.

In case of the Ronchi grating illumination which consists of more spectral orders, the  $+1^{\text{st}}$  order spectrum needs to be separated from the zero and the second order spectra by

$$f_{1\max} < f_{2\min} \quad (2.13)$$

and

$$f_b < f_{1\min}, \quad (2.14)$$

where  $f_b$  is the maximum frequency of the zero-order spectrum.  $f_{(n)\max}$  and  $f_{(n)\min}$  are the maximum and the minimum of the  $n^{\text{th}}$  order components as shown in Figure 2.5, respectively. Substitutions of Eq. (2.12) into Eqs. (2.13) and (2.14) give

$$f_0 + \frac{1}{2\pi} \left| \frac{\partial \varphi(x, y)}{\partial x} \right|_{\max} < 2f_0 - \frac{2}{2\pi} \left| \frac{\partial \varphi(x, y)}{\partial x} \right|_{\max}$$

or

$$\frac{2\pi f_0}{3} > \left| \frac{\partial \varphi(x, y)}{\partial x} \right|_{\max} \quad (2.15)$$

and

$$f_b < f_0 - \frac{1}{2\pi} \left| \frac{\partial \varphi(x, y)}{\partial x} \right|_{\max}, \quad (2.16)$$

respectively. Since in most cases  $f_b$  is much smaller than  $f_0/2$ , the necessary condition for the fundamental spectrum separation is set by Eq. (2.15)

$$\left| \frac{\partial \varphi(x, y)}{\partial x} \right|_{\max} < \frac{2\pi f_0}{3}. \quad (2.17)$$

When  $l_0 \gg h(x, y)$  and  $\varphi(x, y)$  is much larger than  $\varphi_0(x, y)$ , Eq. (2.11) can be simplified as

$$\varphi(x, y) \approx \Delta \varphi(x, y) \approx -\frac{2\pi f_0 d}{l_0} h(x, y). \quad (2.18)$$

Substitution of Eq. (2.18) into Eq. (2.17) gives the maximum value of the slope height measurement

$$\left| \frac{\partial h(x, y)}{\partial x} \right|_{\max} < \frac{l_0}{3d}. \quad (2.19)$$

The conventional FTP can be used only for the surface measurement on which the slopes do not exceed this limitation. When the measurable slope of the height

variation extends the limitation, the fundamental components overlap the zero component and higher components. Aliasing will cause incorrect reconstruction of the object profile as shown in Figure 2.6.

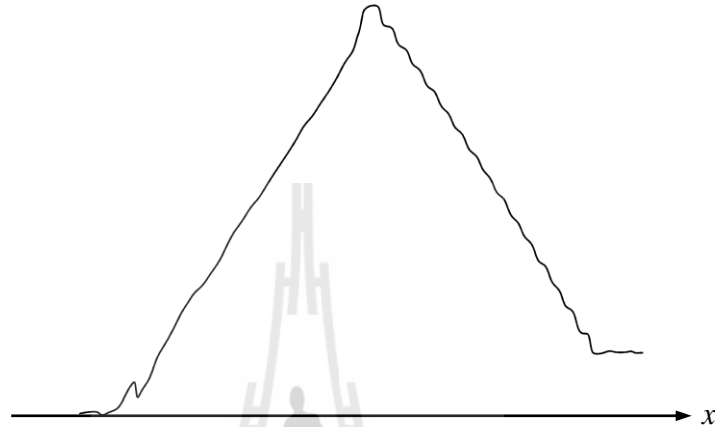


**Figure 2.6** Incorrect reconstruction of the isosceles prism by the conventional FTP.

The preceding discussion reveals that the local spatial frequency of the deformed grating changes with the slope of the height variation. From Eq. (2.18), and Figure 2.1, the rate of change of the phase is related to the slope of (Li, Su, and Guo, 1990)

$$\frac{\partial \phi(x, y)}{\partial x} = -2\pi f_0 \tan \theta \frac{\partial h(x, y)}{\partial x}. \quad (2.20)$$

By substituting Eq. (2.20) into Eq. (2.12), the instantaneous frequency of the +1<sup>st</sup> order frequency spectrum is related to the slope by

$$f_1 \cong f_0 \left[ 1 + \tan \theta \frac{\partial h(x, y)}{\partial x} \right]. \quad (2.21)$$

For the reconstruction of the isosceles prism with the profile shown in Figure 2.7, the triangle side A has the slope of  $\tan \alpha_1$  which is greater than zero, while the slope of

the side B is  $\tan \alpha_2 = -\tan \alpha_1$ . By taking this consideration into account, the instantaneous frequency on the side A can be determined from Eq. (2.21) as

$$f_{1A} = (1 + \tan \theta \tan \alpha_1) f_0. \quad (2.22)$$

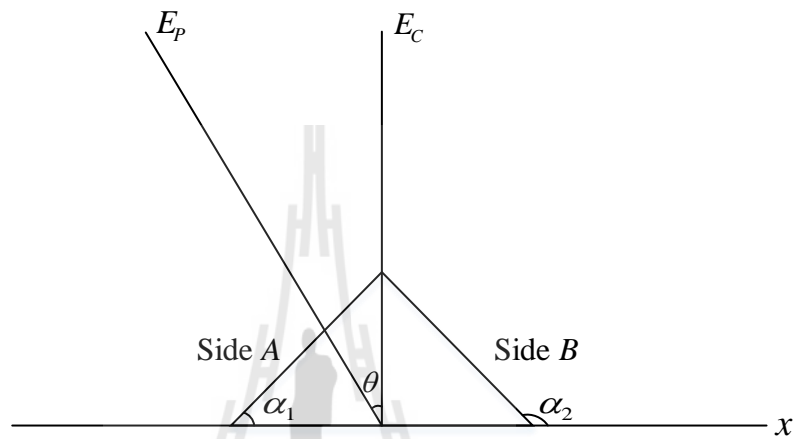


**Figure 2.7** Profile of the isosceles prism.

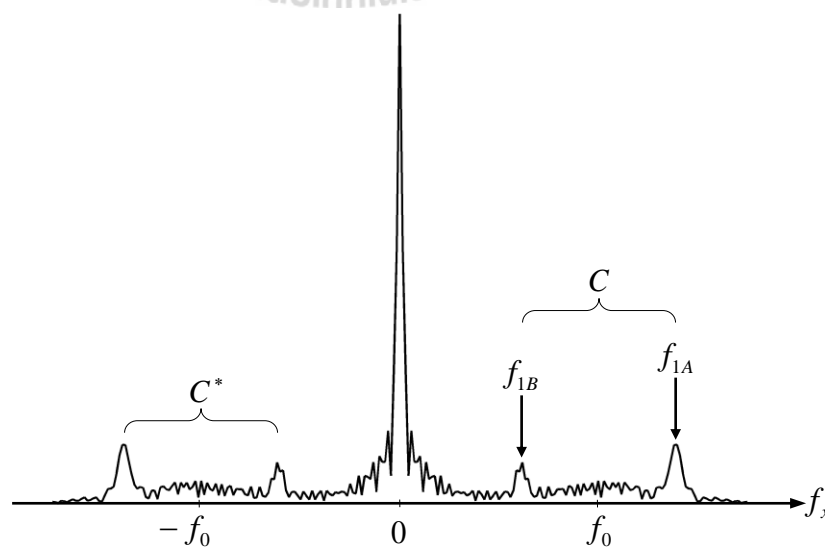


**Figure 2.8** Power spectra of the grating deformed by the isosceles prism.

In the case of the side B, its instantaneous frequency is given by

$$f_{1B} = (1 - \tan \theta \tan \alpha_1) f_0. \quad (2.23)$$

Since  $\tan \alpha_1$  is positive, the instantaneous frequency  $f_{1A}$  and  $f_{1B}$  shown in Figure 2.8 are greater and smaller than the fundamental frequency  $f_0$ . When the two slopes are very high,  $f_{1A} \approx 2f_0$  and  $f_{1B} \approx 0$ . As a result, the 1<sup>st</sup> fundamental and the 0<sup>th</sup> order spectra will overlap.

The spectral overlapping can be partly resolved by the reducing the angle  $\theta$  between the axes of the projector and the CCD. For small  $\theta$ , Eq. (2.18) can be approximately written as  $\Delta\varphi(x, y) \approx -2\pi f_0 \theta h(x, y)$  which shows that the phase shift of the optical field modulated by the height distribution is approximately proportional to  $\theta$ . As a consequence, when  $\theta$  small, only small phase modulation occurs, yielding narrow spectral distribution. However, the smaller  $\theta$  is, the more sensitive  $h(x, y)$  is to  $\Delta\varphi(x, y)$ ,

$$\frac{\partial h}{\partial(\Delta\varphi)} = -\frac{1}{2\pi f_0 \theta}. \quad (2.24)$$

Since this introduces more errors, the measurable slope of the height variation cannot be extended merely by reducing the angle  $\theta$ .

## 2.2 FTP Using $\pi$ -Phase Shifting Method

In the previous section, the limitation of the conventional FTP in measuring objects with high slope or the grating frequency has been discussed. The spectral overlapping makes it difficult to reconstruct the object correctly. In order to solve this limitation, the FTP has been modified by using the  $\pi$ -phase shifting method.

In the modified FTP, the  $\pi$ -phase shifting grating images deformed by the object

$$g_3(x, y) = g_{3dc} + o(x, y) - do(x, y) \cos[2\pi f_0 x + \varphi(x, y)] \quad (2.25)$$

and the reference plane

$$g_4(x, y) = g_{4dc} + r(x, y) - dr(x, y) \cos[2\pi f_0 x + \varphi_0(x, y)] \quad (2.26)$$

are additionally recorded. Intensities scanned at the 100<sup>th</sup> row of the grating images deformed by the object, the object with the  $\pi$ -phase shifting method, the reference-

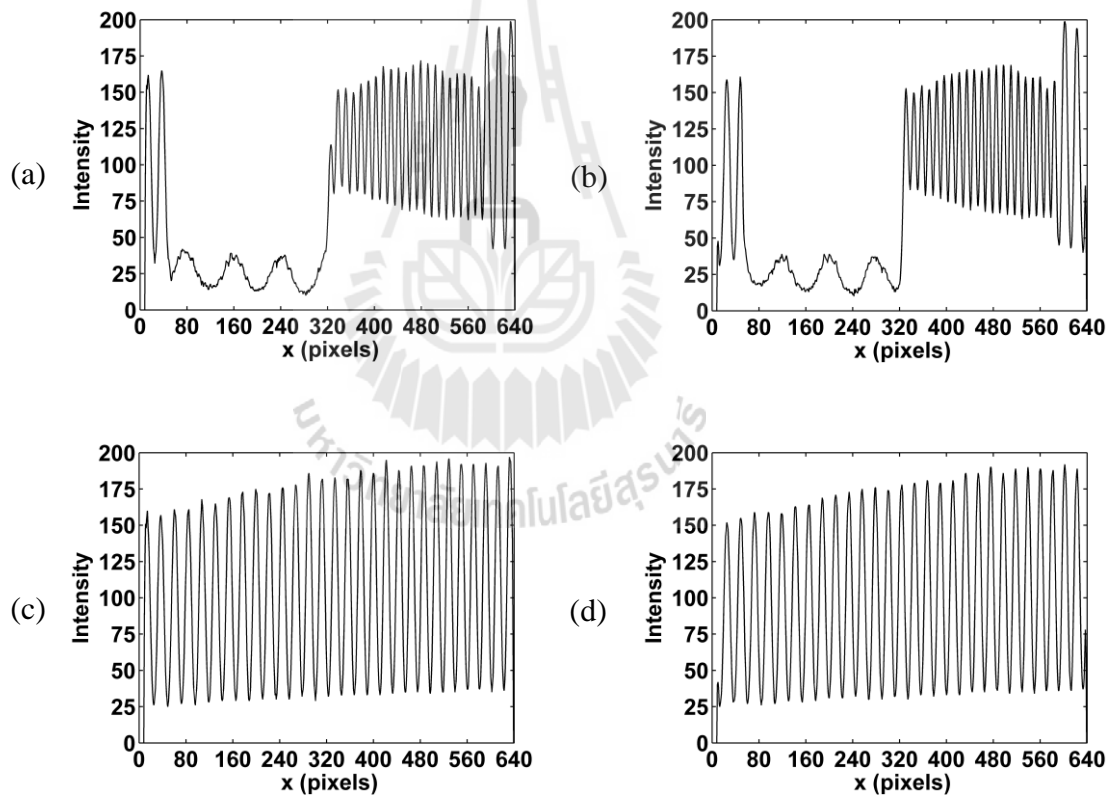


**Figure 2.9** Intensities scanned at the 100<sup>th</sup> row of the grating images deformed by (a) the object, (b) the object with the  $\pi$ -phase shifting method, (c) the reference plane and (d) the reference plane with the  $\pi$ -phase shifting method, respectively.

plane and the reference plane object with the  $\pi$ -phase shifting method are shown in Figures 2.9(a), (b), (c) and (d), respectively. When the dc biases  $g_{1dc} = g_{3dc}$  and  $g_{2dc} = g_{4dc}$ , while the modulation factor  $b = d$ , a subtraction of Eq. (2.25) from Eq. (2.1) gives

$$\begin{aligned} g'(x, y) &= g_1(x, y) - g_3(x, y) \\ &= 2bo(x, y)\cos[2\pi f_0 x + \varphi(x, y)]. \end{aligned} \quad (2.27)$$

Subtracting of Eq. (2.26) from Eq. (2.7) generates

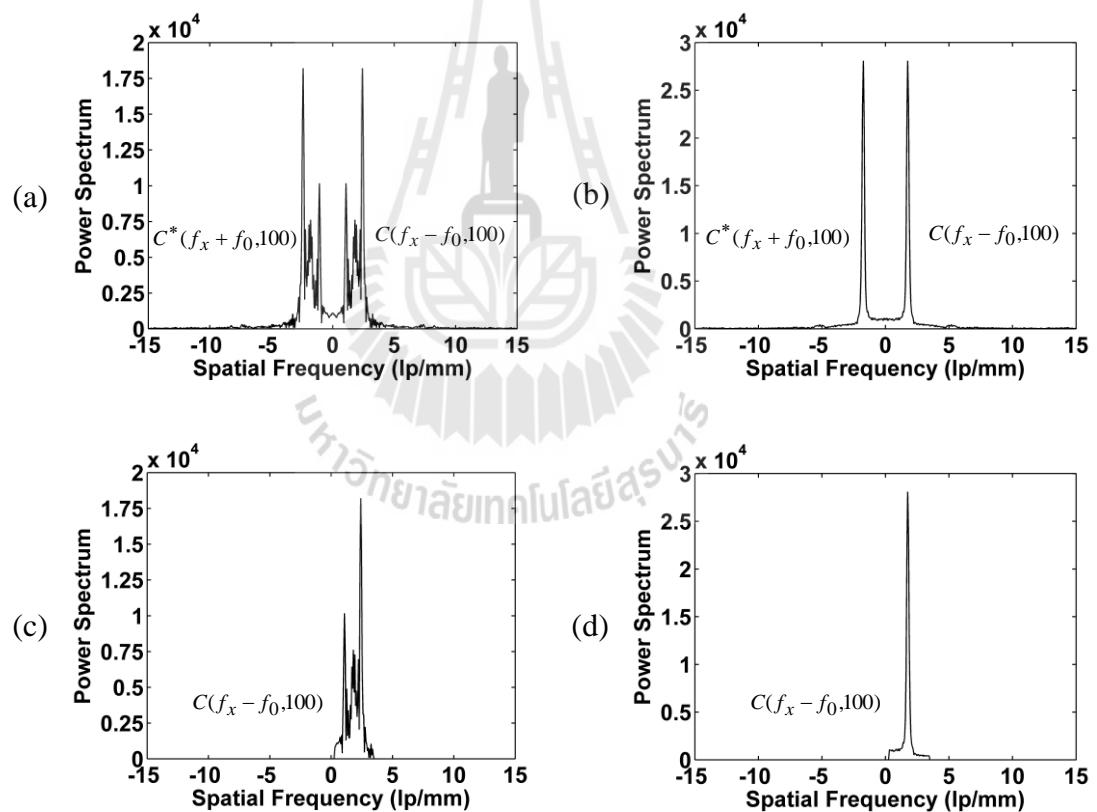


**Figure 2.10** Power spectra of a 1-D signal pattern scanned at the 100<sup>th</sup> row of the grating deformed by (a) the object and (b) the reference plane obtained by using the  $\pi$ -phase shifting method. The filtered +1<sup>st</sup> order spectra  $C(f_x - f_0, 100)$  of (c) Figure a and (d) Figure b, respectively.

$$\begin{aligned}
g''(x, y) &= g_2(x, y) - g_4(x, y) \\
&= 2br(x, y)\cos[2\pi f_0 x + \varphi_0(x, y)]. \quad (2.28)
\end{aligned}$$

Equations (2.27) and (2.28) do not contain the unwanted background or the zeroth order spectrum. Their power spectra are shown in Figures 2.10(a) and (b), respectively. By performing the same operations of the spectral filtering as shown in Figures 2.10(c) and (d), the complex signal

$$g'_3 = bo(x, y)\exp\{i[2\pi f_0 x + \varphi_0(x, y)]\} \quad (2.29)$$

and

$$g'_4 = br(x, y)\exp\{i[2\pi f_0 x + \varphi_0(x, y)]\} \quad (2.30)$$

are generated from Eqs. (2.27) and (2.28), respectively. The complex logarithm of the product of Eq. (2.29) and the complex conjugate of Eq. (2.30) gives the phase difference which can be used to reconstruct the object profile according to Eq. (2.11).

When the modified FTP employs the sinusoidal grating, the second order spectrum vanishes. Consequently, Eq. (2.13) reduce to  $f_{1\max} < 2f_0$ , yielding

$$\left| \frac{\partial \varphi(x, y)}{\partial x} \right| < 2\pi f_0. \quad (2.31)$$

By substituting Eq. (2.18) into Eq. (2.31), the measurable slope becomes

$$\left| \frac{\partial h(x, y)}{\partial x} \right| < l_0 / d, \quad (2.32)$$

which is three times higher than the conventional FTP.

## CHAPTER III

### BACKGROUND ELIMINATION METHOD

In this chapter, a new method for improving the 3-D surface reconstruction of the FTP by using the background elimination is proposed. The proposed method can be implemented by using the same optical setup used to implement the conventional FTP. Besides projecting the grating pattern, the LCD projector is also used to produce uniform light.

#### 3.1 Introduction

A new method for improving performance of the FTP using a background elimination is implemented. Unlike the  $\pi$ -phase shifting method (Li, Su, and Guo, 1990), the backgrounds  $o(x, y)$  and  $r(x, y)$  can be determined from images of the object and the reference plane generated by using uniform light. The use of the uniform light illumination has advantages over the  $\pi$ -phase shifting method in that firstly, the phase deviation of the periodic grating pattern caused by the projector jitter may be obviated by minimizing the number of the projected gratings patterns. Secondly, time delay for projecting the  $\pi$ -phase shifting grating pattern is reduced. However, due to unbalanced light distribution caused by the grating pattern and the uniform light, a dc component of each recorded image will be different. Therefore, in

order to remove effectively the background, the dc bias of each captured image must also be eliminated.

### 3.2 FTP Using Background Elimination Method

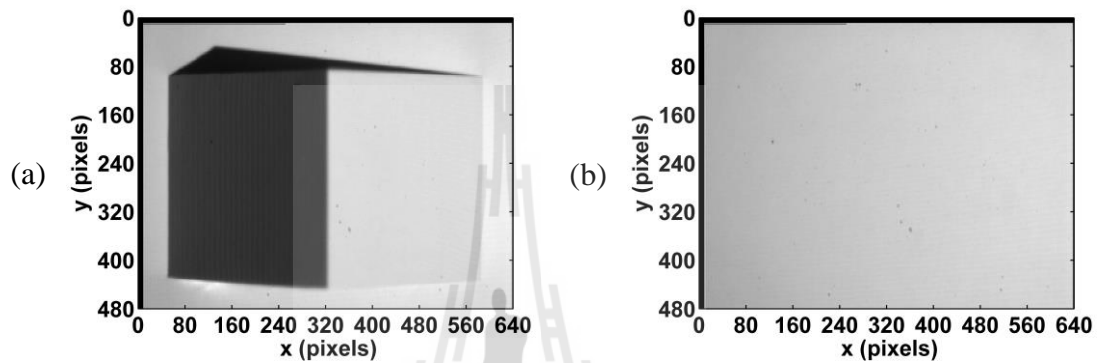


**Figure 3.1** Images of (a) the isosceles prism and (b) the flat reference plane obtained by using the uniform light illumination, respectively.

Figures 3.1(a) and (b) show the recorded images of the same isosceles prism and the reference plane produced by using the uniform light which can be expressed as

$$g_3(x, y) = c_r' [g_{3dc} + o(x, y)] \quad (3.1)$$

and

$$g_4(x, y) = c_r'' [g_{4dc} + r(x, y)], \quad (3.2)$$

respectively.  $c_r'$  corresponds to the contrast ratio of the object images generated by using the grating and the uniform light illuminations, while  $c_r''$  is for the contrast ratio of the reference plane images obtained with the same kind of light illuminations.

The contrast of each image is defined as (Peli, 1990)

$$c = \frac{\int \int_{-\infty}^{+\infty} |G(f_x, f_y)| df_x df_y}{|G(0,0)|}, \quad (3.3)$$

where  $G(f_x, f_y)$  corresponds to the amplitude spectrum of the image, while  $G(0,0)$  is the zero frequency. The unwanted backgrounds are then eliminated by the following operations

$$\begin{aligned} g'(x, y) &= g_1(x, y) - g_{1dc} - [g_3(x, y) - g_{3dc}] / c_r' \\ &= bo(x, y) \cos[2\pi f_0 x + \varphi(x, y)] \end{aligned} \quad (3.4)$$

and

$$\begin{aligned} g''(x, y) &= g_2(x, y) - g_{2dc} - [g_4(x, y) - g_{4dc}] / c_r'' \\ &= br(x, y) \cos[2\pi f_0 x + \varphi_0(x, y)]. \end{aligned} \quad (3.5)$$

Here,  $g_{mdc}(x, y)$  is the dc bias of the  $m^{\text{th}}$  recorded image calculated by

$$g_{mdc} = \frac{1}{A} \iint_R g_m(x, y) dA \quad (3.6)$$

with  $A$  is the area of the region  $R$ . The division of the second terms in Eqs. (3.4) and (3.5) by the contrast ratios are used to equalize the ac component of the images generated by the grating and the uniform illuminations. This ensures that the unwanted backgrounds are completely eliminated and the desired phase information encoded into the fundamental spectra can be extracted by using the Fourier transformation.

Figures 3.2(a) and (b) show the intensities scanned at the 100<sup>th</sup> row of the grating images deformed by the object and the reference plane, respectively, while Figures 3.2(c) and (d) show the object and the reference plane images, respectively. It is clear that both amplitude and phase of the grating patterns are modulated by the

profiles of the object and the reference plane. Due to different reflectivities and surface heights, the four images have different dc bias levels.

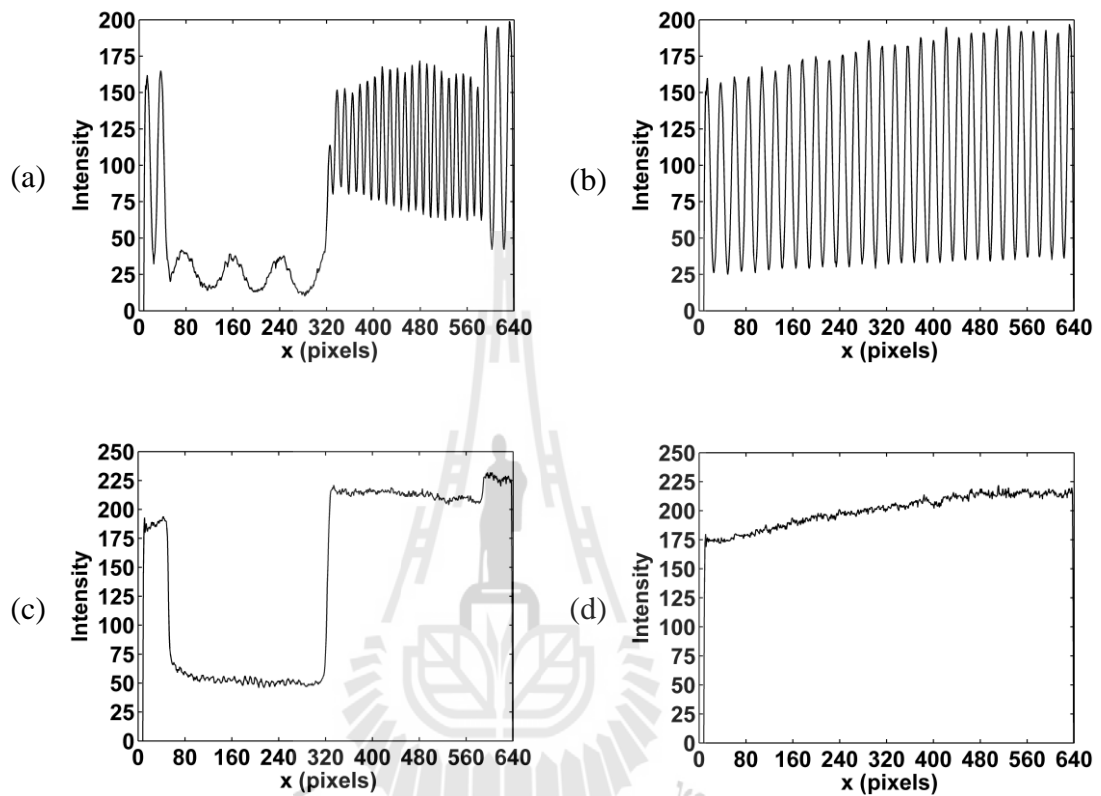


**Figure 3.2** Intensities scanned at the 100<sup>th</sup> row of the grating images deformed by (a) the object and (b) the reference plane. Intensities scanned at the 100<sup>th</sup> row of the images of (c) the object and (d) the reference plane, respectively.

Figures 3.3(a) and (b) show the intensities of the deformed grating images with the dc bias removal of  $g_1(x,100) - g_{1dc}$  and  $g_2(x,100) - g_{2dc}$ , respectively. The intensities of the object and the reference plane images obtained by the dc removal of  $[g_3(x,100) - g_{3dc}] / c_r$  and  $[g_4(x,100) - g_{4dc}] / c_r$  are shown in Figures 3.3(c) and (d),

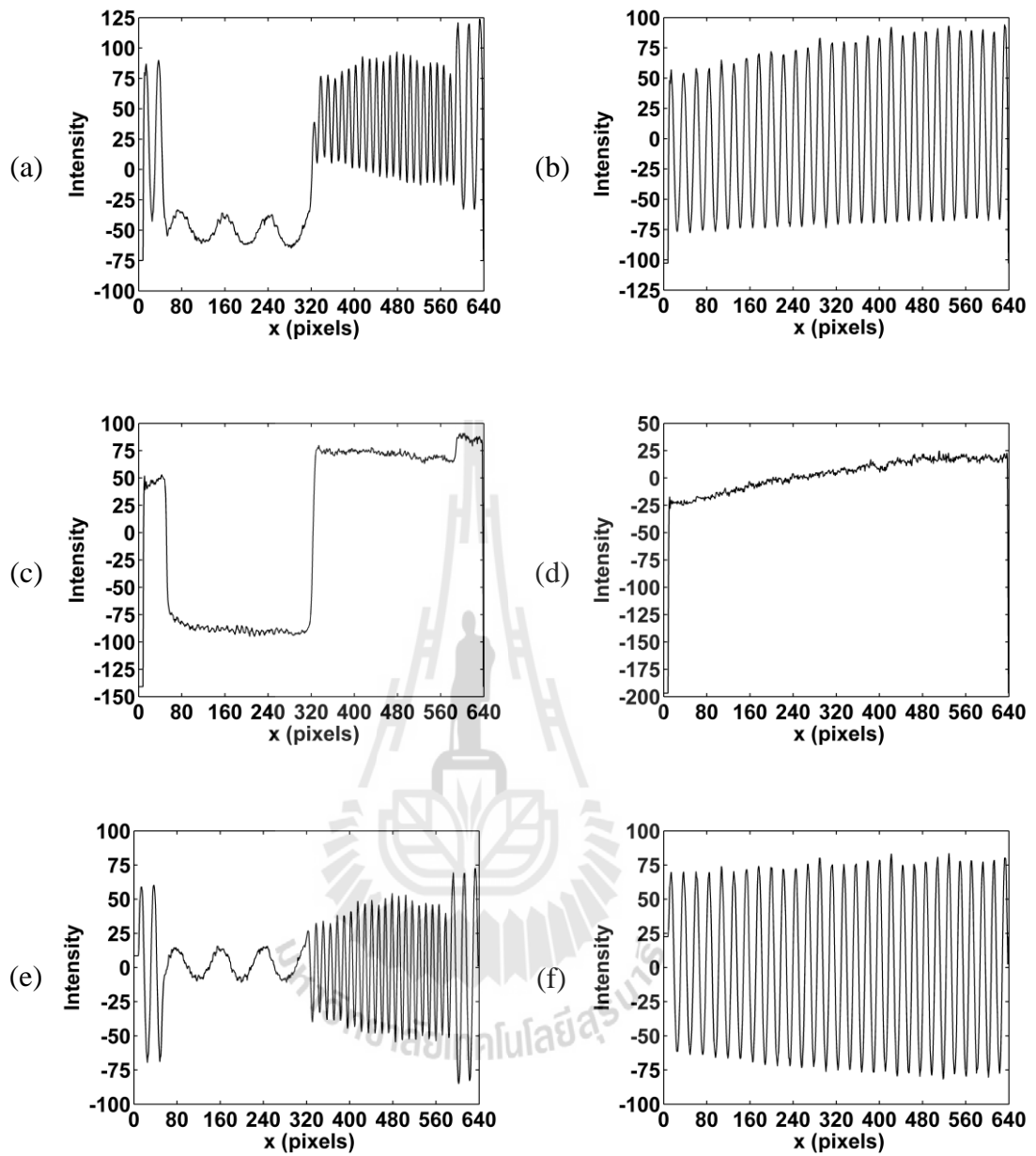


**Figure 3.3** Intensities scanned at the 100<sup>th</sup> row of (a)  $g_1(x,100) - g_{1dc}$ , (b)  $g_2(x,100) - g_{2dc}$ , (c)  $[g_3(x,100) - g_{3dc}] / c_r'$ , (d)  $[g_4(x,100) - g_{4dc}] / c_r''$ , (e) Eq. (3.4) and (f) Eq. (3.5), respectively.

respectively. These figures show that the resultant amplitude intensities do not symmetrically vary with respect to the zero level because of the nonuniform

reflections of the object and the reference plane. The resultant background elimination obtained by computing Eqs. (3.4) and (3.5) are shown in Figures 3.3(e) and (f). Besides having the zero dc biases, the amplitude intensities are now symmetrically distributed.

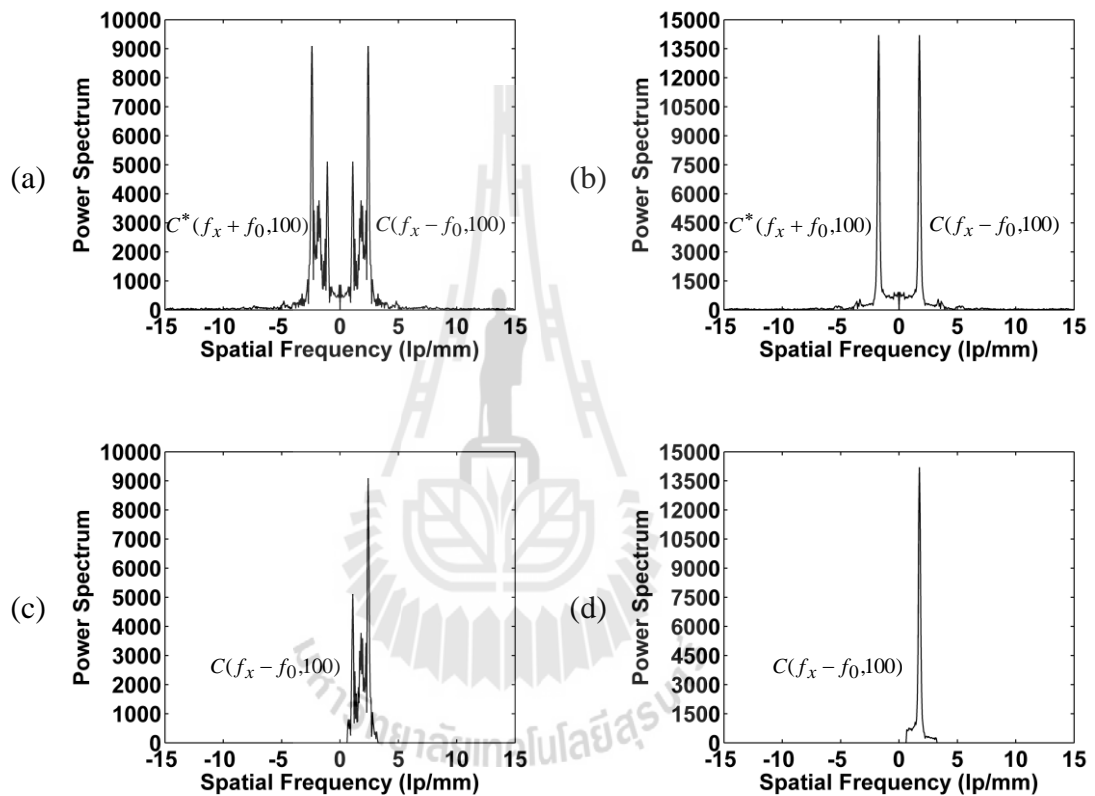


**Figure 3.4** Power spectra of the grating pattern deformed by (a) the object and (b) the reference plane which are obtained by eliminating the unwanted background. The filtered  $+1^{st}$  order spectra  $C(f_x - f_0, 100)$  of (c) Figure (a) and (d) Figure (b), respectively.

Figures 3.4(a) and (b) correspond to the power spectra of the two signals shown in Figures 3.3(e) and (f), respectively. It is obvious from this figure that the

first order spectra with broad spectral width can be easily identified. In the conventional FTP, besides its high amplitude and broad spectral width, the presence of the zeroth-order spectrum causes problem in localizing the fundamental spectra. By filtering only a single fundamental spectrum as shown in Figures 3.4(c) and (d) and taking its inverse Fourier transform, Eqs. (3.4) and (3.5) reduce to

$$g'(x, y) = 0.5bo(x, y) \exp\{i[2\pi f_0 x + \varphi(x, y)]\} \quad (3.7)$$

and

$$g''(x, y) = 0.5br(x, y) \exp\{i[2\pi f_0 x + \varphi_0(x, y)]\}, \quad (3.8)$$

respectively. The phase difference  $\varphi(x, y) - \varphi_0(x, y)$  can be extracted by taking a complex logarithm of the product of Eq. (3.7) and the conjugate of Eq. (3.8)

$$\begin{aligned} \log\{g'(x, y) \cdot g''^*(x, y)\} = \log\{0.25b^2 o(x, y)r(x, y)/c', c''\} \\ + i[\varphi(x, y) - \varphi_0(x, y)]. \end{aligned} \quad (3.9)$$

while the height distribution is calculated by  $h(x, y)$  in Eq. (2.11).

## CHAPTER IV

### EXPERIMENTAL VERIFICATIONS

In this chapter, experimental verifications of the proposed background elimination method is discussed. Isosceles prism and arbitrary-shaped objects are used as test specimens. The isosceles prism is used to calibrate the system and to verify the improvement of the proposed method. The experimental results are compared with those of the conventional and the  $\pi$ -phase shifting method based modified FTPs.

#### 4.1 Experimental Setup

In order to verify feasibility of the proposed method, the optical setup for implementing the 3-D shape measurement shown in Figure 4.1 was constructed. Isosceles prisms with the dimensions of 133.51 mm  $\times$  70.1 mm  $\times$  42.71 mm and 133.12 mm  $\times$  70.1 mm  $\times$  81.24 mm and a 600 ml plastic water bottle shown in Figures 4.2(a), (b) and (c) were employed as the test objects, respectively. The first prism had the slope of 0.64, while the second one was 1.22. These object dimensions were measured by using a digital height gauge (Moore and Wright, MW190-30DBL) with an accuracy of 0.01 mm. A LCD projector (Toshiba, TLP-X2000) with resolution 1024  $\times$  768 pixels was used to project the sinusoidal grating and the uniform white patterns. The grating patterns with the pitch  $p$  of 3.24 mm and 4.84 mm were generated by using the Matlab program (R2009a). The grating images

deformed by the object and the reference plane were recorded by using a CCD camera (Hamamatsu, C5948) having the resolution of  $640 \times 480$  pixels in the area of  $8.3 \text{ mm} \times 6.3 \text{ mm}$ . Lens (AF Nikkor,  $f=50\text{mm}$ ,  $f/1.4\text{D}$ ) was used to produce images on the CCD sensor, which were saved into tiff format. The distance  $l_0$  between the optical axes and the reference plane was  $1050 \text{ mm}$ , while the lens magnification was about 19 times. The reconstruction performance of the proposed background elimination was verified at the angle  $\theta$  of  $4^\circ$  and  $28^\circ$ . According to these angles, the grating pitch  $p_0$  at the reference plane can be calculated by using

$$p_0 = \frac{P}{\cos\theta} . \quad (4.1)$$



**Figure 4.1** Optical setup for implementing the FTP.

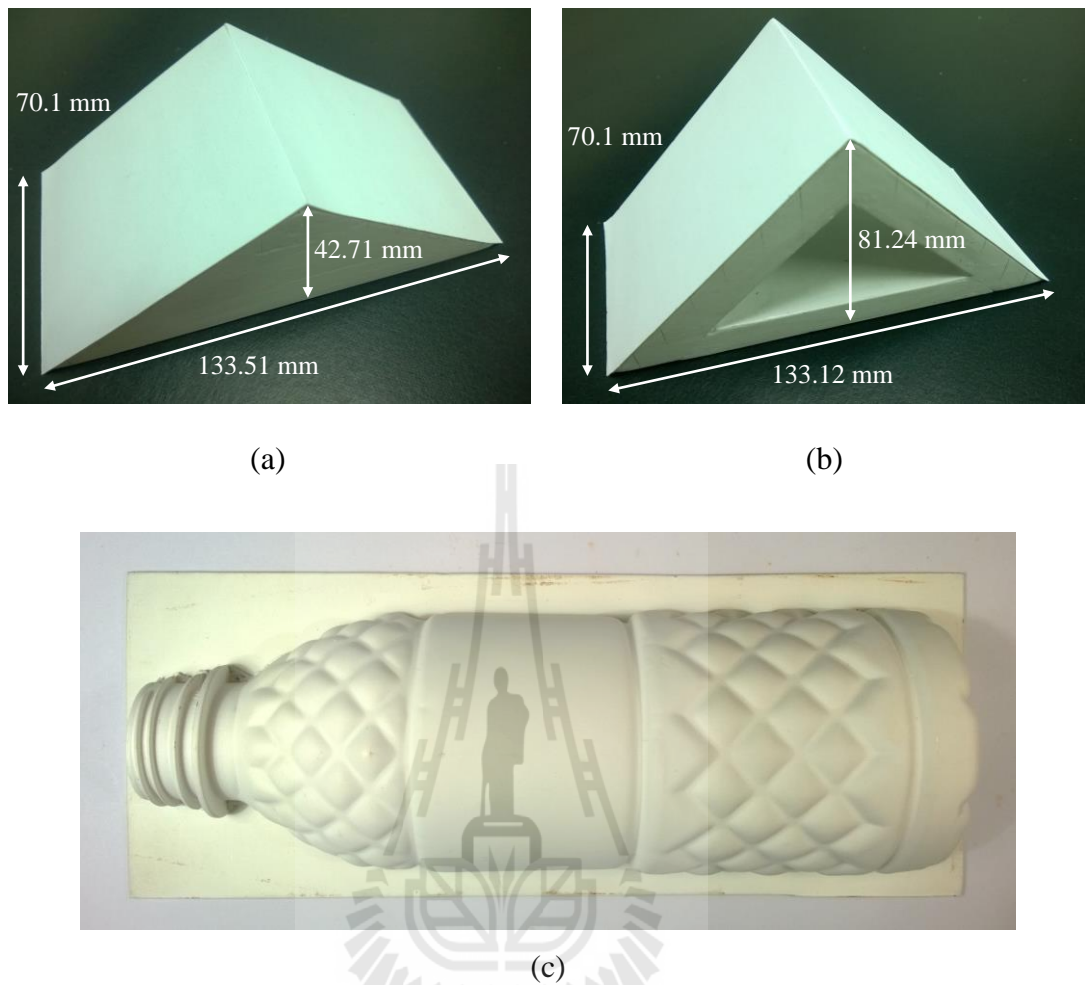


**Figure 4.2** Two isosceles prism with the heights of (a) 42.71 mm, (b) 81.24 mm and (c) a 600 ml plastic water bottle, respectively.

**Table 4.1** The grating pitch  $p_0$  of the proposed FTP as a function of the angle  $\theta$ .

Angle $\theta$ ( $^\circ$ )	Grating pitch $p_0 = p/\cos\theta$ (mm)	
	$p = 3.24$ mm	$p = 4.84$ mm
4	3.25	4.85
28	3.67	5.48

Table 4.1 shows the non-linear variation of grating pitch as a function of the angle  $\theta$  between the camera and the projector axes.

## 4.2 Calibration of the Distances $l_0$ and $d$

In order to have high accuracy in the 3-D surface reconstruction, the distances  $l_0$  and  $d$  were calibrated by measuring two isosceles prism at the same angle  $\theta$ . For the maximum height position, Eq. (2.11) can be rewritten as

$$l_0 = h(x, y)_{\max} - h(x, y)_{\max} \left\{ \frac{[2\pi d / p_0]}{\Delta\phi(x, y)_{\max}} \right\}, \quad (4.2)$$

where  $h(x, y)_{\max}$  and  $\Delta\phi(x, y)_{\max}$  are the maximum height of the prism and its corresponding phase difference, respectively. The value of  $h(x, y)_{\max}$  can be accurately measured by using the digital height gauge, while  $\Delta\phi(x, y)_{\max}$  is obtained from the numerical calculations.  $l_0$  and  $d$  can be calculated by using Eq. (4.2) for two maximum heights. The calibration gave the average distance  $l_0 = 1050$  mm. Table 4.2 shows the distance  $d$  and the maximum measurable slope of the conventional and the proposed FTPs as a function of the angle  $\theta$ .

**Table 4.2** The distance  $d$  and the maximum measurable slope of the proposed FTP.

Angle $\theta$ (°)	$d$ (mm)	Maximum slope	
		Conventional FTP	Proposed FTP
4	72.48	4.82	14.48
28	558.29	0.62	1.88

### 4.3 Algorithm of the Proposed FTP Method

A block diagram of the 3D surface reconstruction by using the proposed FTP is shown in Figure 4.3. Firstly, the grating patterns  $g_1$  and  $g_2$  deformed by the object and the reference plane were recorded. The images of the object and the reference plane,  $g_3$  and  $g_4$ , were subsequently recorded. Secondly, the dc signal and the contrast of each image were calculated, together with their contrast ratios. Thirdly, the backgrounds were eliminated and the desired first-order spectra were generated through the FFT. Fourthly, the phase difference was calculated and unwrapped. Finally, the surface profile was reconstructed.

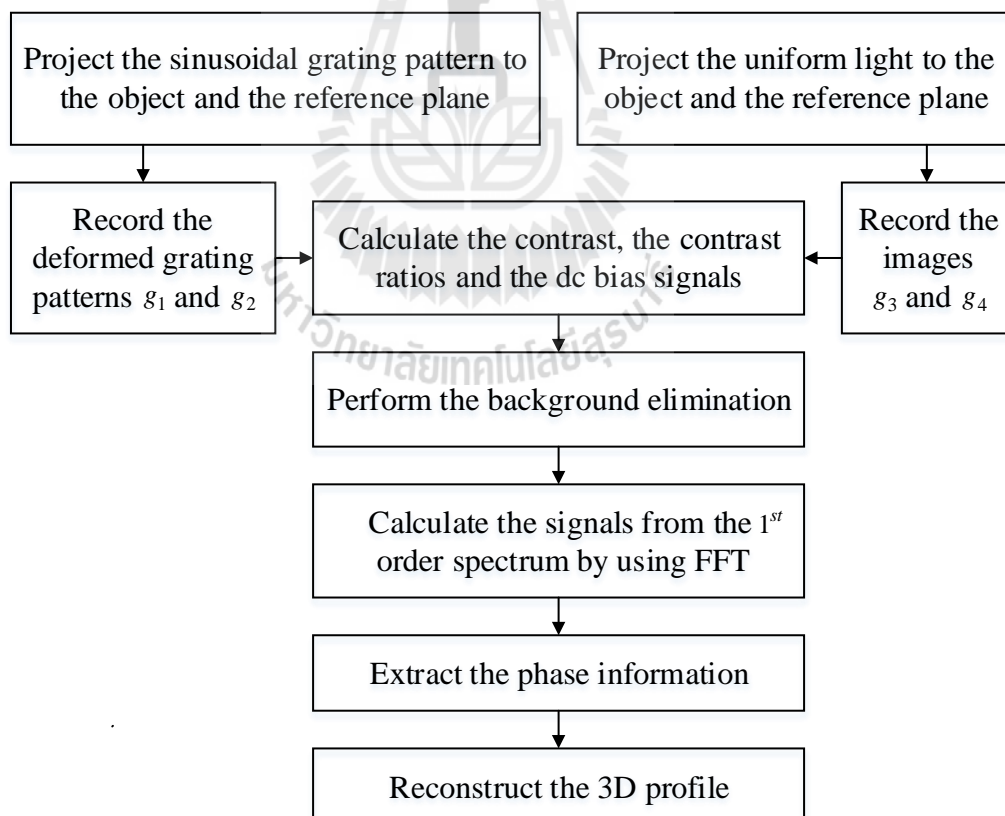


**Figure 4.3** A block diagram of a numerical calculation for the surface reconstruction by using the background elimination method.

## 4.4 Results and Discussions

### 4.4.1 Isosceles Prism Object with Low Slope

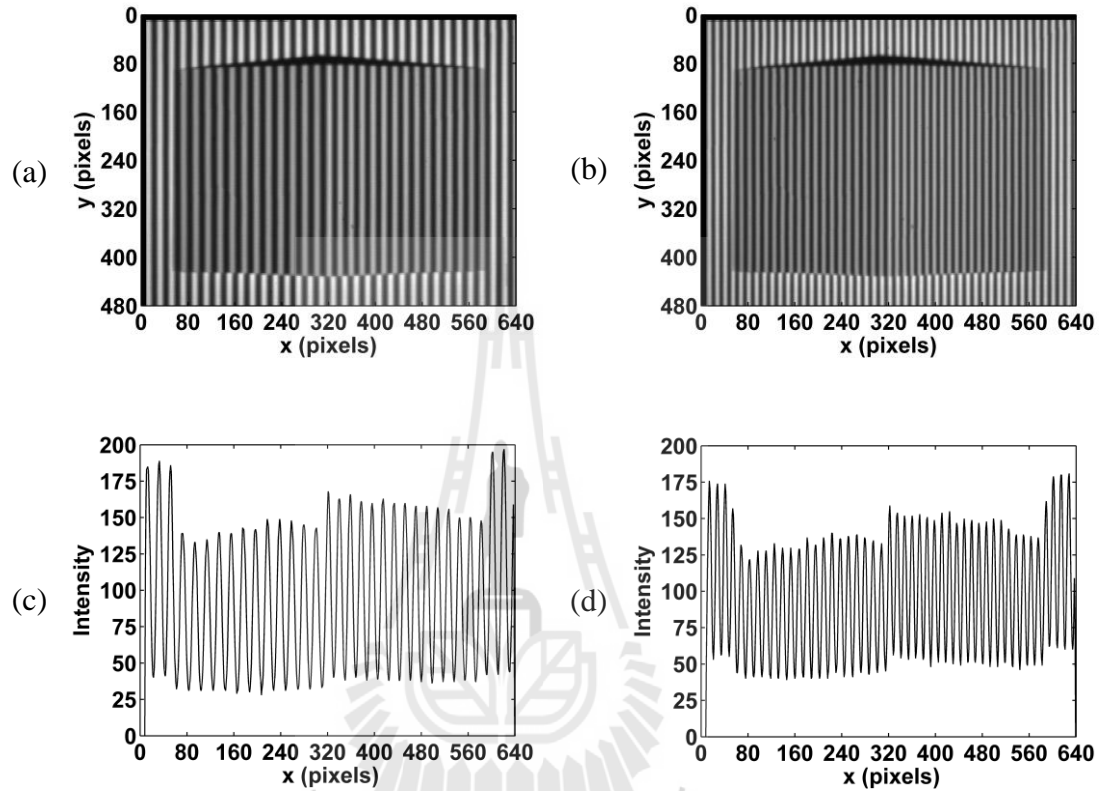


**Figure 4.4** Images of the grating pattern deformed by the isosceles prism with the slope 0.64 in situation that the projected gratings have the pitch of (a) 4.84 mm and (b) 3.24 mm at the angle  $\theta = 4^\circ$ . Intensities scanned at the 100<sup>th</sup> row of (c) Figure (a) and (d) Figure (b), respectively.

Figures 4.4(a) and (b) show the grating patterns deformed by the isosceles prism with the slope 0.64 at the angle  $\theta = 4^\circ$ . Figure 4.4(a) corresponds to the projection of the grating with the pitch  $p = 4.84$  mm, while Figure 4.4(b) is for the pitch  $p = 3.24$  mm. Black areas appeared immediately on top of the pattern

deformed by the object correspond to the shadows. The intensities scanned at the 100<sup>th</sup> row of the corresponding grating images shown in Figures 4.4(a) and (b) are presented in Figures 4.4(c) and (d), respectively. It can be seen that due to broader pitch of the projected grating, the intensities of the deformed grating pattern in Figure 4.4(c) is higher than that of Figure 4.4(d). The difference of the phase modulation by the two sides of the prism is hardly observed, because orientation of the two sides with respect to the projector axis are almost equal. The signals with higher amplitude which appear on the left and the right sides are produced by the reference plane which has white color. Thus, its reflection is higher than the object.

Figures 4.5(a) and (b) show the deformed grating patterns obtained when the angle  $\theta$  is increased to  $28^\circ$ . As the angle becomes bigger, the projected grating pattern is incident on the left side of the prism at a bigger angle than on the right side. As a consequence, the intensity and the pitch of the deformed gratings on the left side shown in Figures 4.5(c) and (d) become lower and broader, respectively. The same effect of using broader pitch of the projected grating can be seen in Figure 4.5(c) that is the intensity becomes higher than in Figure 4.5(d). As a result, the deformed grating pattern has non-uniform background. Furthermore, in comparison with Figure 4.5(c), Figure 4.5(d) reveals that there is discontinuity around the middle of the signal. This is because the height around the peak position compressed the grating pattern. When the grating pitch is narrow, the compressed grating pattern cannot be resolved by the imaging system of the camera. As a result, wrong phase modulation is encoded into the deformed grating.

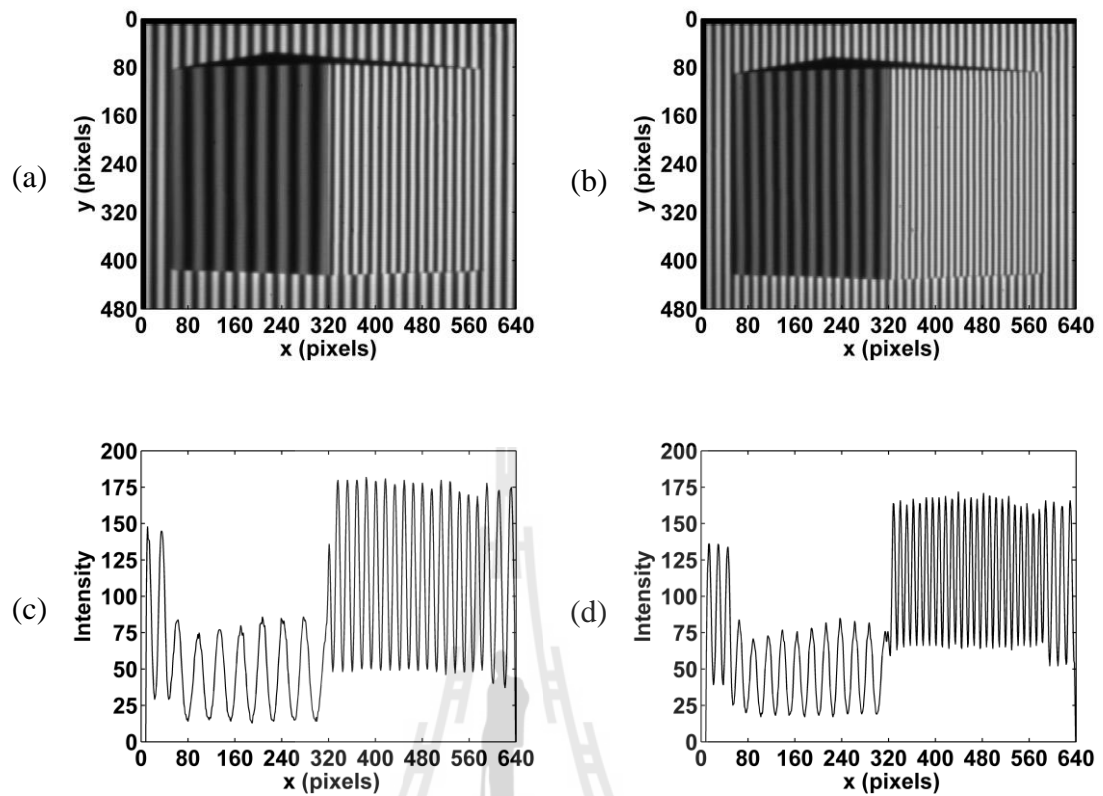


**Figure 4.5** Images of the grating pattern deformed by the isosceles prism with the slope 0.64 in situation that the projected gratings have the pitch of (a) 4.84 mm and (b) 3.24 mm at the angle  $\theta = 28^\circ$ . Intensities scanned at the 100<sup>th</sup> row of (c) Figure (a) and (d) Figure (b), respectively.

By applying our proposed method to the deformed grating patterns, the non-uniform background can be totally eliminated. The resultant background elimination from the deformed gratings shown in Figures 4.4(a) and (b) are depicted in Figures 4.6(a) and (b), while Figures 4.6(c) and (d) are the results from the gratings in Figures 4.5(c) and (d), respectively. Due to the elimination of the background signal, the deformed gratings have almost symmetric positive and negative intensities.

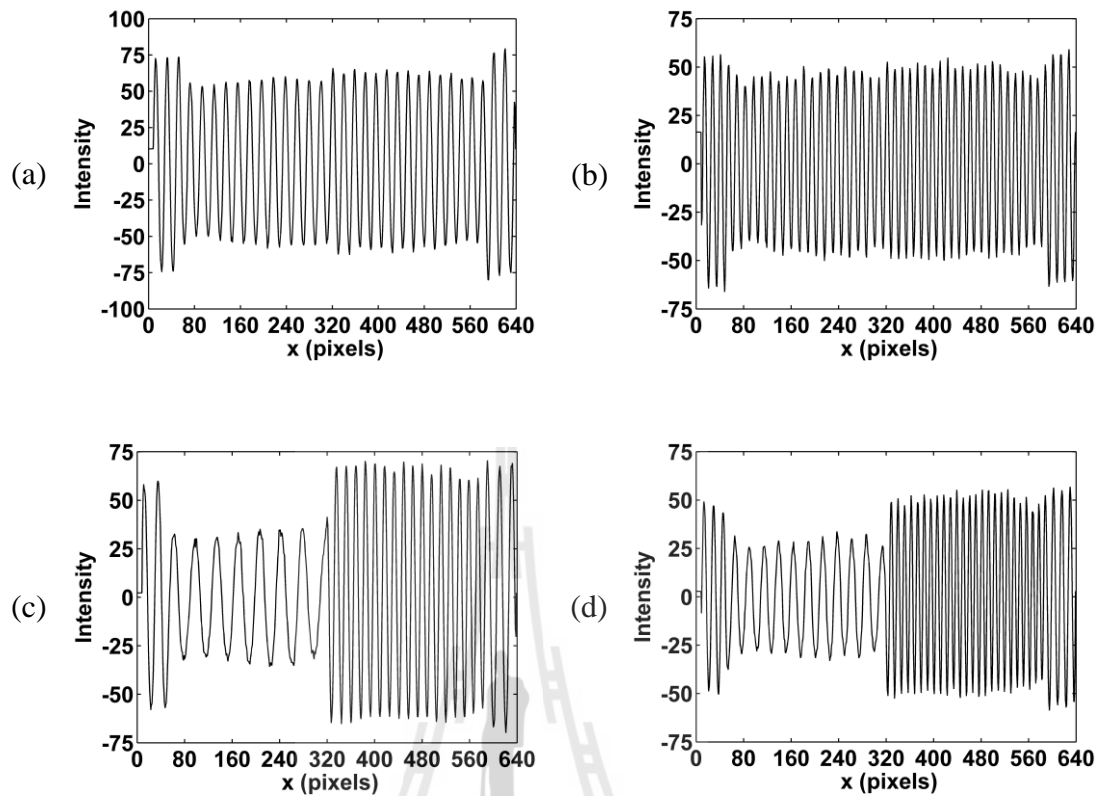


**Figure 4.6** Intensities scanned at the 100<sup>th</sup> row of the background eliminated grating patterns obtained from (a) Figure 4.4(a), (b) Figure 4.4(b), (c) Figure 4.5(a) and (d) Figure 4.5(b), respectively.

Power spectra of the background eliminated grating patterns in Figures 4.6(a), (b), (c) and (d) are shown in Figures 4.7(a), (b), (c) and (d), respectively. It is obvious from this figure that the first-order spectra can be easily identified. Due to the bigger angle, the first-order spectra shown in Figures 4.7(c) and (d) have broader spatial frequency components than Figures 4.7(a) and (b). These are in agreement with Eqs. (2.22) and (2.23).

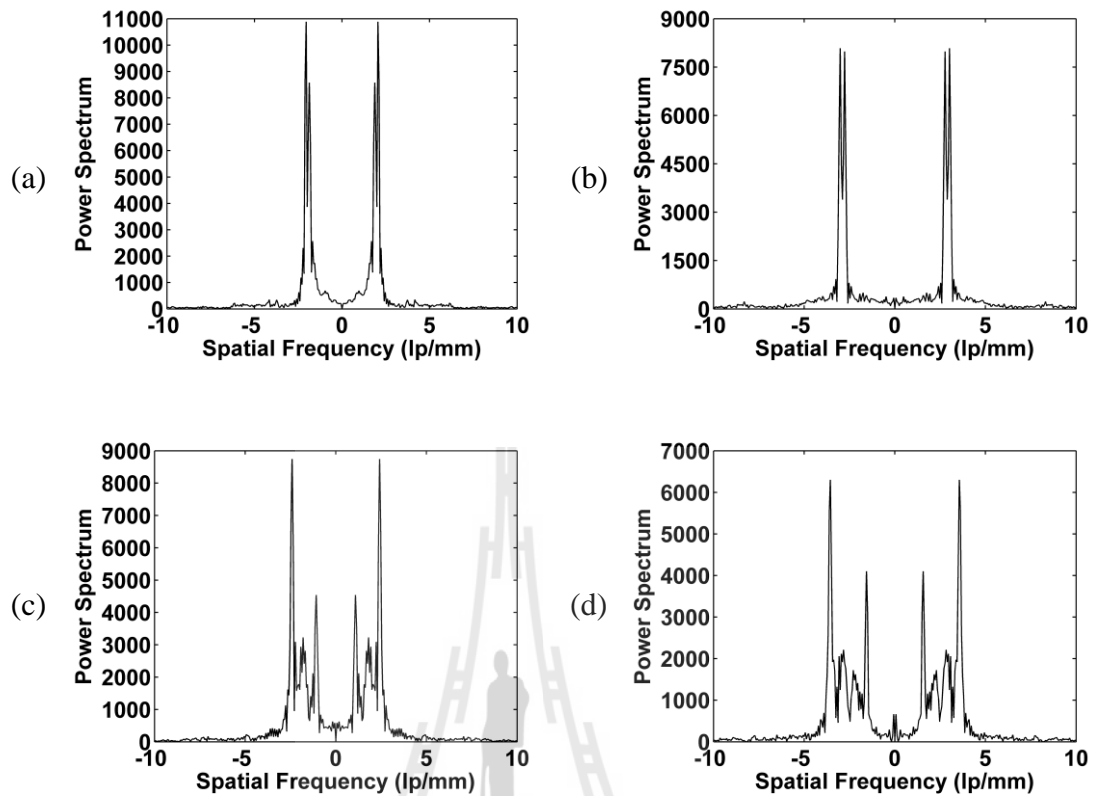


**Figure 4.7** Power spectra of the background eliminated grating patterns obtained from (a) Figure 4.6(a), (b) Figure 4.6(b), (c) Figure 4.6(c) and (d) Figure 4.6(d), respectively.

Figure 4.8 plots the reconstructed height profiles of this isosceles prism obtained by using the conventional, the modified and the proposed FTPs. They are compared with the height measured by using the digital height gauge. Figures 4.8(a) and (b) corresponds to the heights reconstructed at the angle  $\theta = 4^\circ$  by using the grating pitches of 4.84 mm and 3.24 mm, respectively. The passbands of the filters used to reconstruct the height profiles shown in Figures 4.8(a) and (b) were 0.542~3.253 lp/mm and 2.048~3.855 lp/mm, respectively. The resultant heights reconstructed at the angle  $\theta = 28^\circ$  by using the same gratings are shown in Figures-

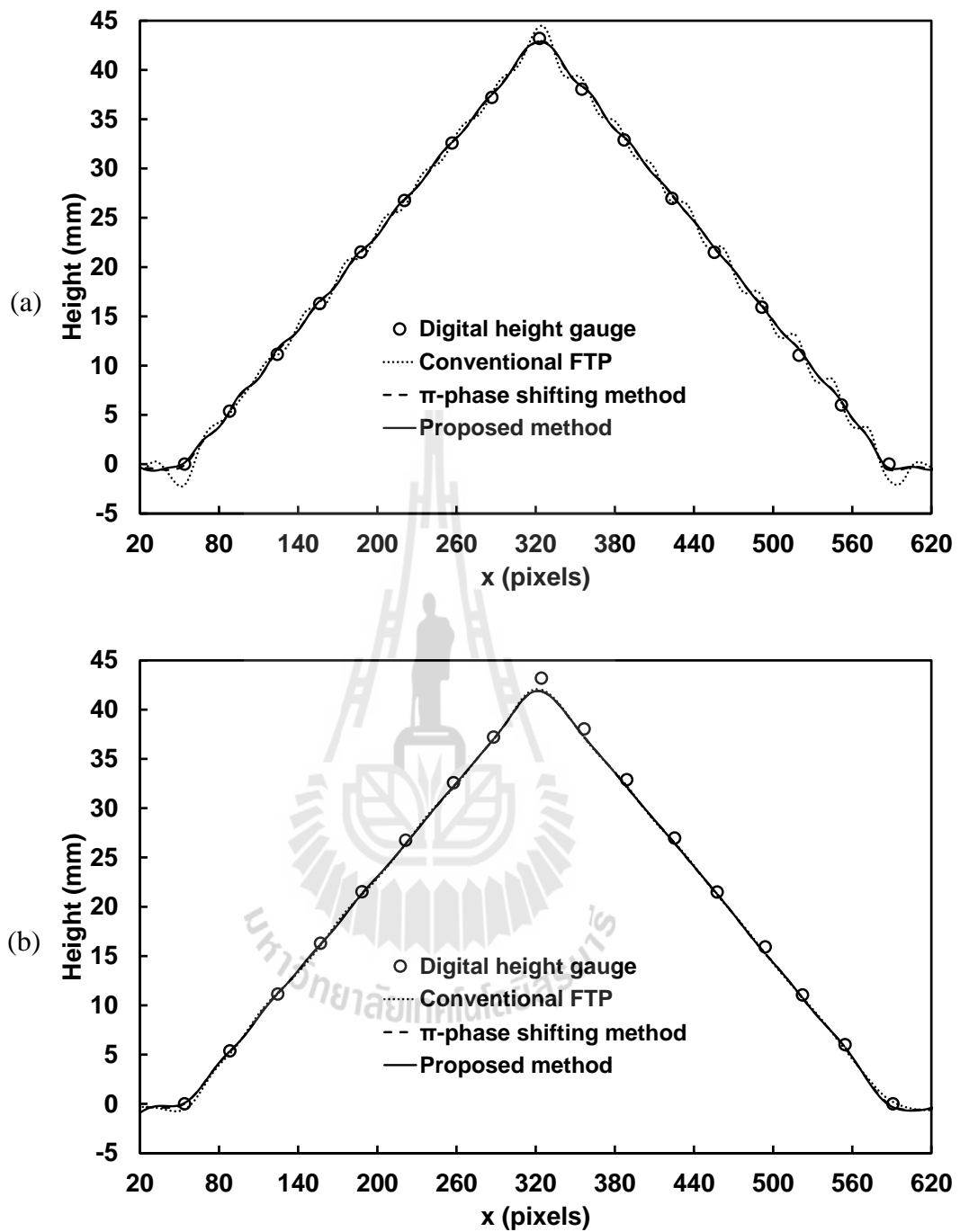


**Figure 4.8** Height profiles of the isosceles prism with the slope of 0.64 reconstructed at the angle  $\theta = 4^\circ$  by using the conventional, the  $\pi$ -phase shifting and the proposed FTPs compared with the digital height gauge in situation that the gratings have the pitch of (a) 4.84 mm and (b) 3.24 mm, respectively.

4.9(a) and (b). Since the angle is larger, Figure 4.9(a) is obtained by using the filter with the passband of 0.361~4.217 lp/mm, while Figure 4.9(b) is 0.301~5.542 lp/mm. The results were the average value of the 63 reconstructed heights. The circle symbol denotes the height measured by the digital gauge. The dot, the broken and the solid lines represent the heights obtained by the conventional, the modified and the proposed FTPs, respectively. It can be seen that the conventional FTP has considerable errors when the grating pitch is low or the angle  $\theta$  is big. This is because the instantaneous  $f_{1B}$  of the first-order spectrum overlaps with the zero-order spectrum. However, regardless of the  $\theta$ , the heights reconstructed by the modified and the proposed FTPs with the grating pitch of 4.84 mm are closer to the actual height than those by the pitch of 3.24 mm. The maximum and the minimum of the reconstruction errors by using the grating pitch of 4.84 mm are 1.914% and 0.152%, respectively. This may be caused by the discontinuous phase at the prism peak which cannot give the correct peak height. Finally, it is found that the height along two sides of the prism reconstructed at the angle  $\theta = 28^\circ$  varies straighter than those at  $\theta = 4^\circ$ . This is because the bigger angle  $\theta$  encodes broader spatial-frequency component, yielding finer reconstruction. Therefore, the proposed FTP by using the background elimination method has the same reconstruction accuracy as the  $\pi$ -phase shifting FTP.

The 3-D height reconstructed at  $28^\circ$  by using the  $\pi$ -phase shifting and the proposed method with the grating pitch of 4.84 mm is shown in Figures 4.10(a) and (b), respectively. For the sake of clarity, the number of pixels in the  $x$  and the  $y$  axes are reduced. It is obvious that the reconstructed height profile corresponds to the isosceles prism.

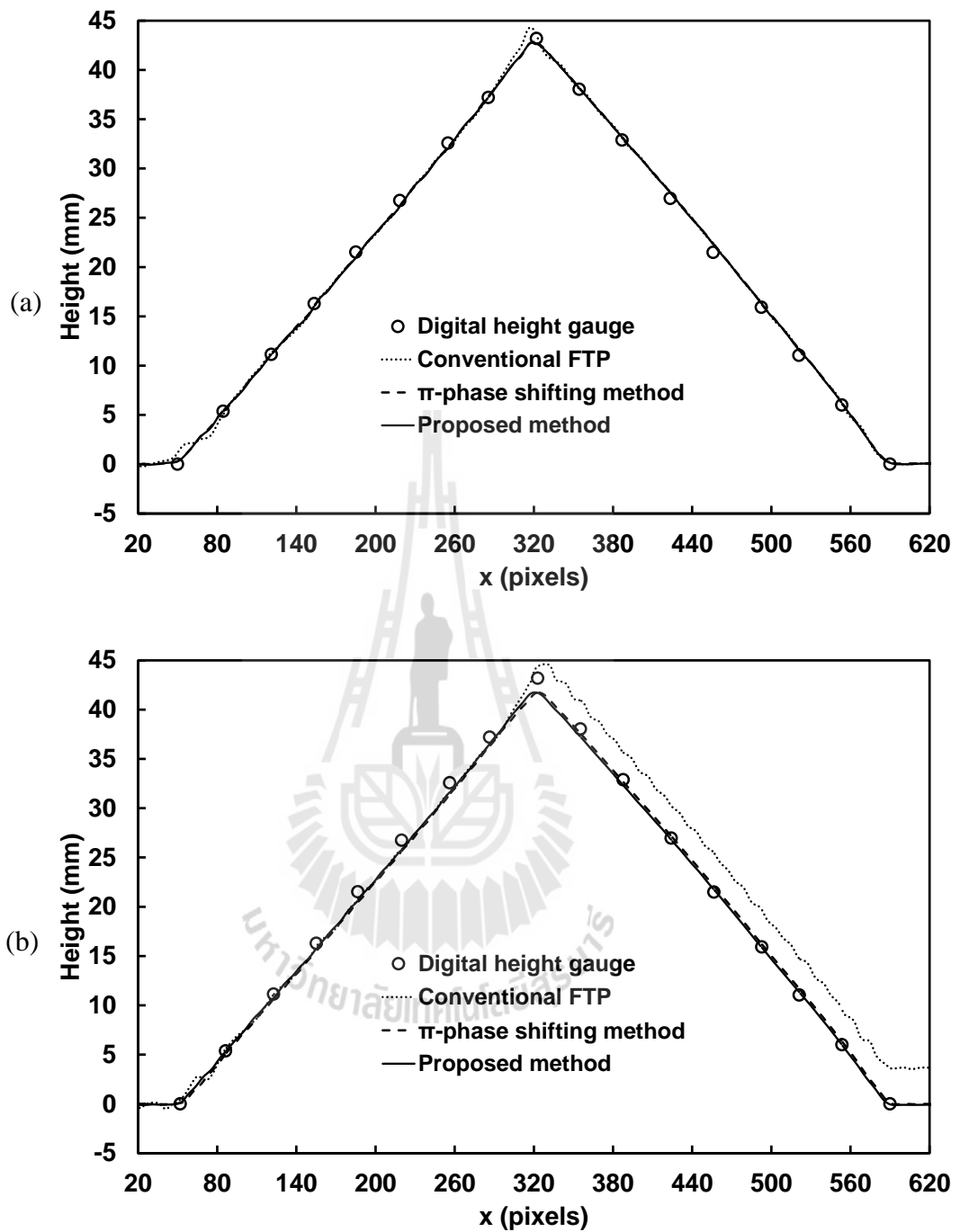


**Figure 4.9** Height profiles of the isosceles prism with the slope of 0.64 reconstructed at the angle  $\theta = 28^\circ$  by using the conventional, the  $\pi$ -phase shifting and the proposed FTPs compared with the digital height gauge in situation that the gratings have the pitch of (a) 4.84 mm and (b) 3.24 mm, respectively.

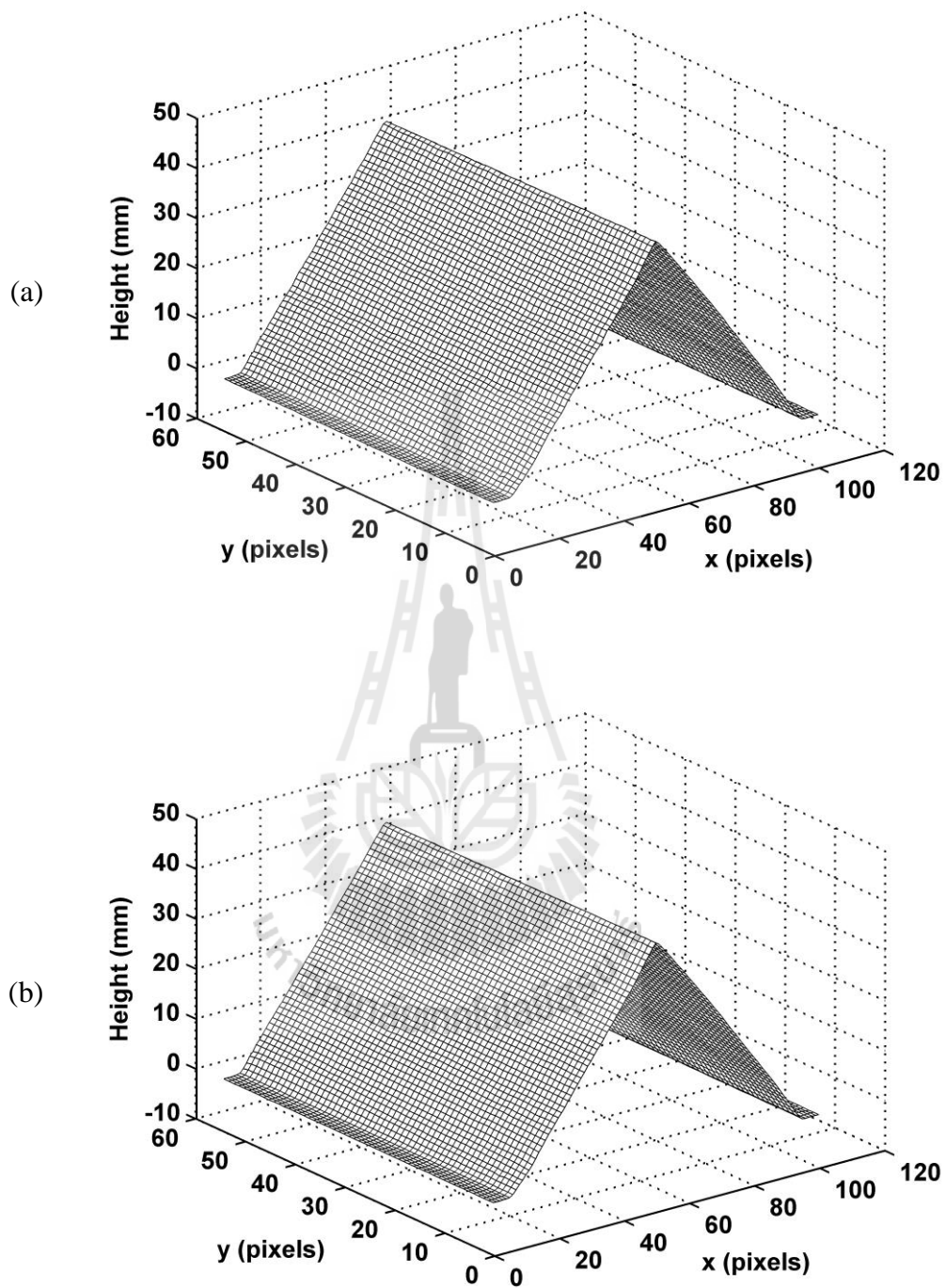


**Figure 4.10** 3-D height profile of the isosceles prism reconstructed in situation that the projected grating has the pitch of 4.84 mm at the angle  $\theta = 28^\circ$  by using (a) the  $\pi$ -phase shifting and (b) the proposed methods, respectively.

#### 4.4.2 Isosceles Prism Object with High Slope

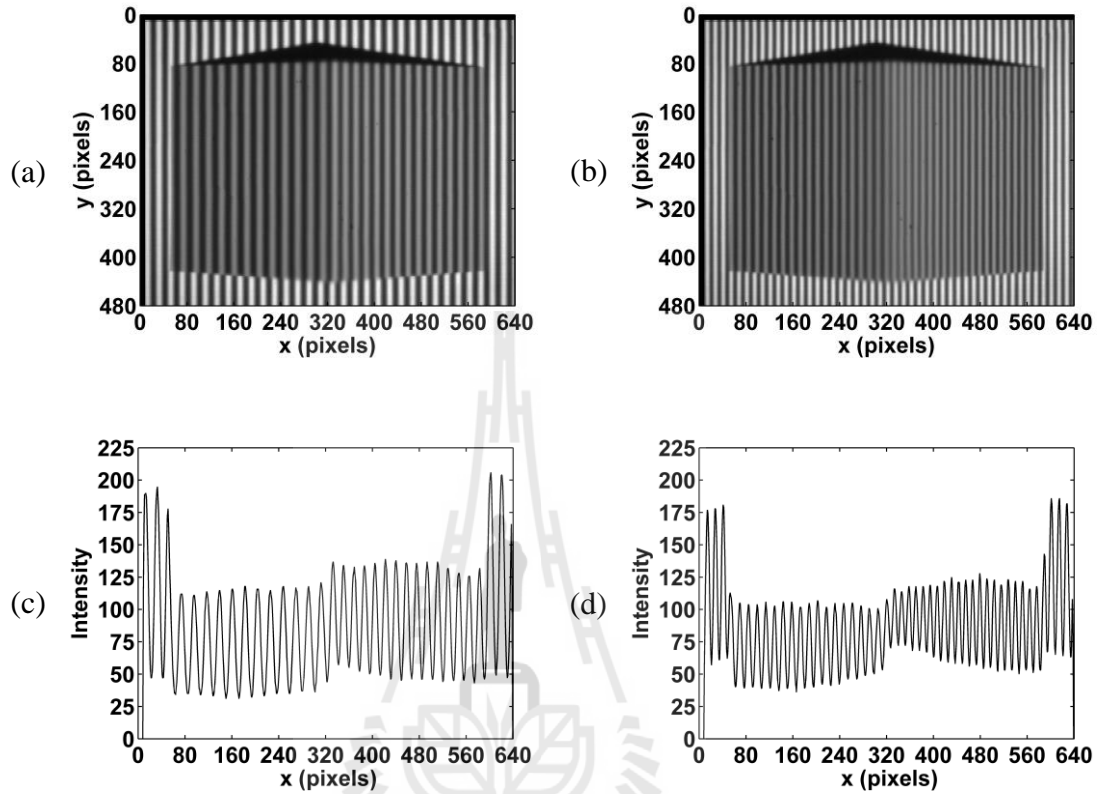


**Figure 4.11** Images of the grating pattern deformed by the isosceles prism with the slope 1.22 in situation that the projected gratings have the pitch of (a) 4.84 mm and (b) 3.24 mm at the angle  $\theta = 4^\circ$ . Intensities scanned at the 100<sup>th</sup> row of (c) Figure (a) and (d) Figure (b), respectively.

The second verification of the proposed method was the height reconstruction of the isosceles prism with the slope of 1.22 at the same angle  $\theta = 4^\circ$  and  $28^\circ$ . The images of the deformed grating patterns with the pitch of 4.84 mm and 3.24 mm are shown in Figures 4.11(a) and (b), respectively. The corresponding intensities scanned at the 100<sup>th</sup> row are shown in Figures 4.11(c) and (d), respectively.

Similar results as the ones discussed in Section. 4.4.1 are obtained. However, the intensities reflected by the object have smaller magnitude, because when the slope is two times higher the incident grating pitch is narrower.

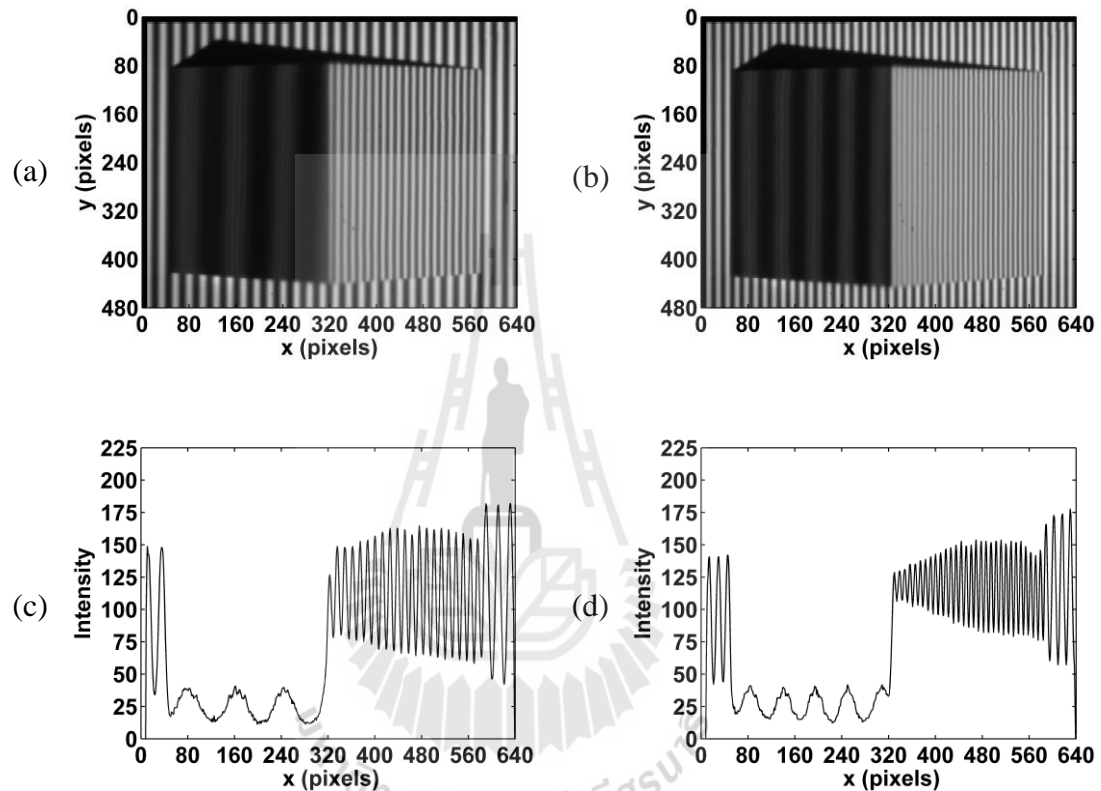


**Figure 4.12** Images of the grating pattern deformed by the isosceles prism with the slope 1.22 in situation that the projected gratings have the pitch of (a) 4.84 mm and (b) 3.24 mm at the angle  $\theta = 28^\circ$ . Intensities scanned at the 100<sup>th</sup> row of (c) Figure (a) and (d) Figure (b), respectively.

When the angle  $\theta$  becomes  $28^\circ$ , the same effect of different elongation on the projected grating causes the left side of the object produce lower intensity and broader pitch than the right one. These can be clearly observed from the deformed

gratings shown in Figures 4.12(a) and (b) and also from their corresponding intensities in Figures 4.12(c) and (d), respectively. In summary, when the object has high slope, the background level and the spatial frequency difference between the left and the right sides vary significantly. As the consequence, the overlapping of the first and the zero-order spectra may cause significant problem in the 3-D surface reconstruction.

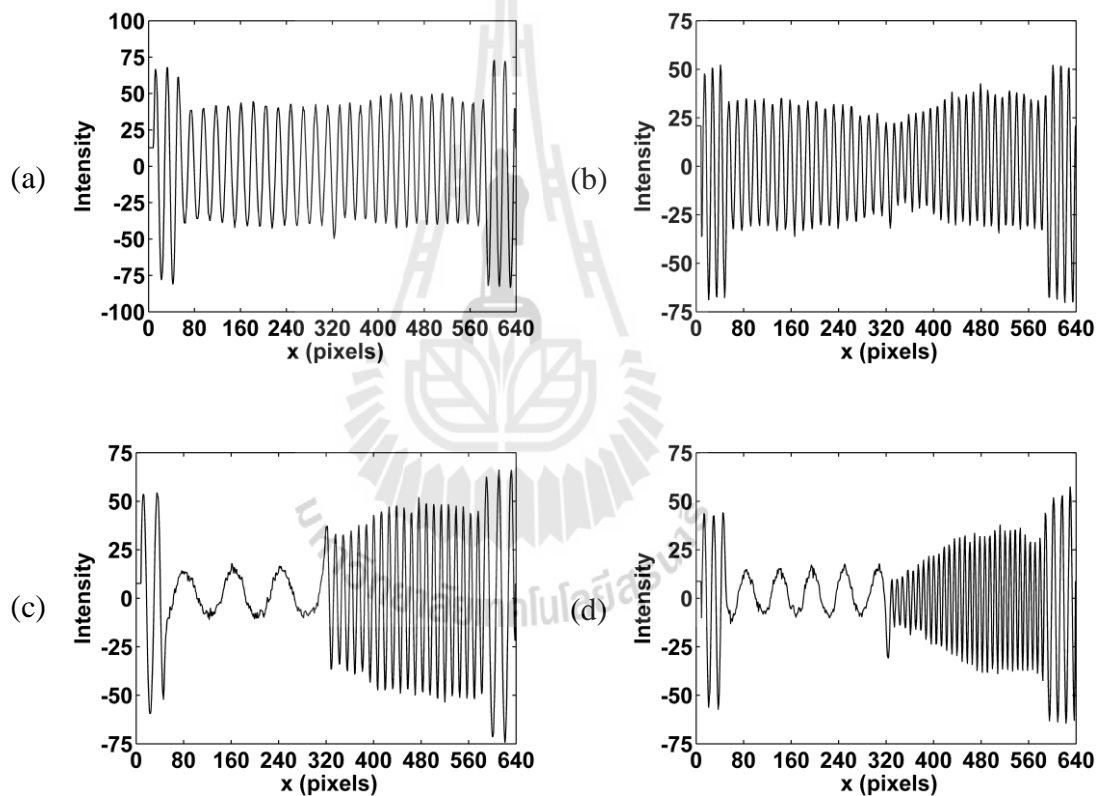


**Figure 4.13** Intensities scanned at the 100<sup>th</sup> row of the background eliminated grating patterns obtained from (a) Figure 4.11(a), (b) Figure 4.11(b), (c) Figure 4.12(a) and (d) Figure 4.12(b), respectively.

Figures 4.13(a), (b), (c) and (d) show the resultant intensities after applying the proposed background elimination from Figures 4.11(a), (b), Figures

4.12(a) and (b), respectively. It is obvious that our proposed method can eliminate effectively the background signal which varies rapidly. The resultant intensities have symmetrical magnitude with respect to the zero level. The power spectra of the background eliminated grating patterns illustrated in Figures 4.13(a), (b), (c) and (d) are shown in Figures 4.14(a), (b), (c) and (d), respectively. It is obvious that the zeroth-order spectra corresponding to the background information can be totally eliminated. In comparison with Figures 4.7, it is clear that due to the higher object slope, the first-order spectra have broader spectral widths.

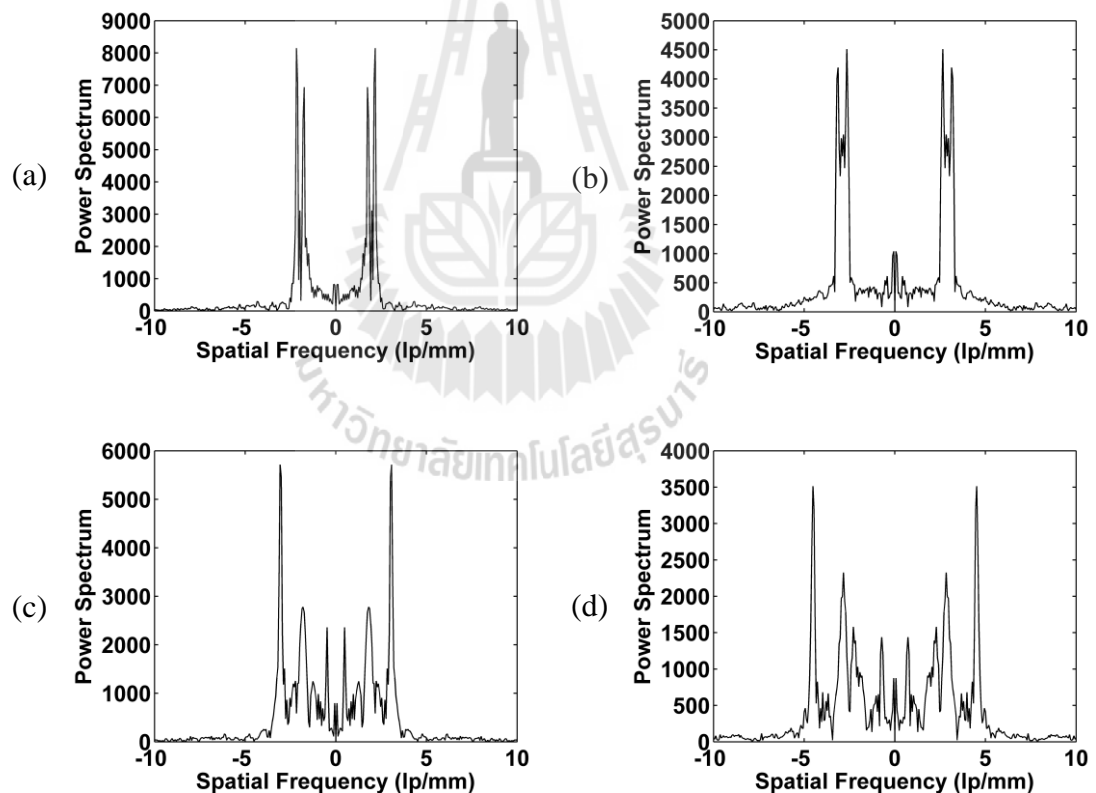


**Figure 4.14** Power spectra of the background eliminated grating patterns obtained from (a) Figure 4.13(a), (b) Figure 4.13(b), (c) Figure 4.13(c) and (d) Figure 4.13(d), respectively.

The plots of the height profile of the isosceles prism with the slope 1.22 reconstructed at the angle  $\theta = 4^\circ$  by the grating pitches of 4.84 mm and 3.24 mm are shown in Figures 4.15(a) and (b), respectively. The filter used in Figure 4.15(a) had the passband of 0.963~3.554 lp/mm, while Figure 4.15(b) was 1.867~4.639 lp/mm. Unlike the conventional FTP, the  $\pi$ - phase shifting method and the proposed FTPs give more accurate result. These results verify that the proposed method has higher measurable slope. In the case of the reconstruction at the angle  $\theta = 28^\circ$ , the results by using the two gratings are shown in Figures 4.16(a) and (b). In Figure 4.16(a), the filter had the passband 0.241~4.759 lp/mm. Figure 4.16(b) was obtained by using the passband of 0.120~6.145 lp/mm. It is clear that the reconstruction by the conventional FTP has serious error. This is because the first-order spectrum overlaps with the zero-order one. The use of the projected grating with the pitch of 3.24 mm gives the similar tendency of reconstruction error at the prism peak. Therefore, the reconstruction error of the grating with the broad pitch is smaller than that of the narrow one. The maximum and the minimum of the reconstruction errors by using the grating pitch of 4.84 mm are 1.067% and 0.137%, respectively.

Figure 4.17 shows the 3-D height profile of the isosceles prism reconstructed by using the proposed method with the grating pitch of 4.84 mm and the angle  $\theta$  of  $28^\circ$ . It is clear that the height profiles of the isosceles prism with the high slope can be reconstructed without using the  $\pi$ -phase shifting method.

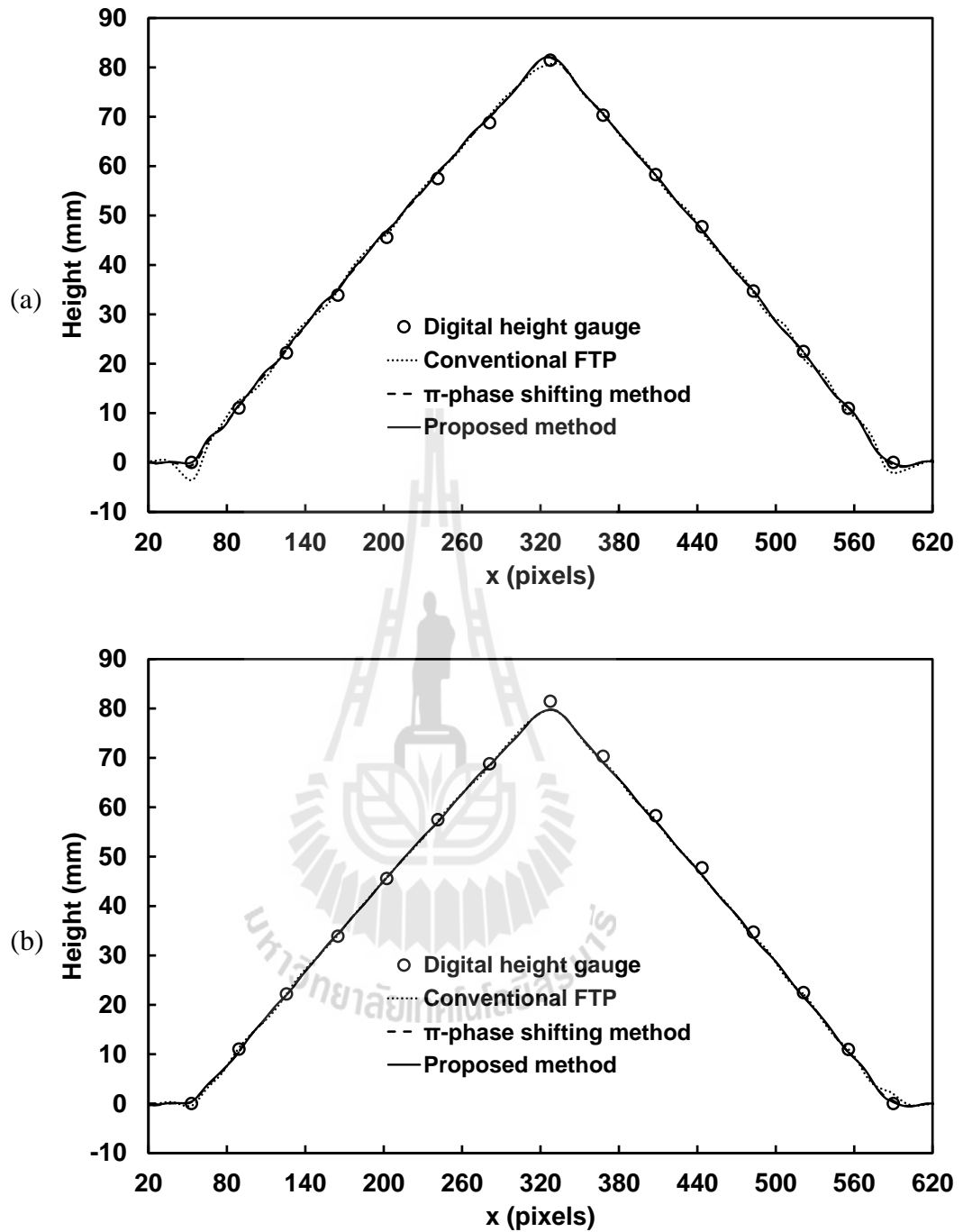


**Figure 4.15** Height profiles of the isosceles prism with the slope of 1.22 reconstructed at the angle  $\theta = 4^\circ$  by using the conventional, the  $\pi$ -phase shifting and the proposed FTPs compared with the digital height gauge in situation that the gratings have the pitch of (a) 4.84 mm and (b) 3.24 mm, respectively.

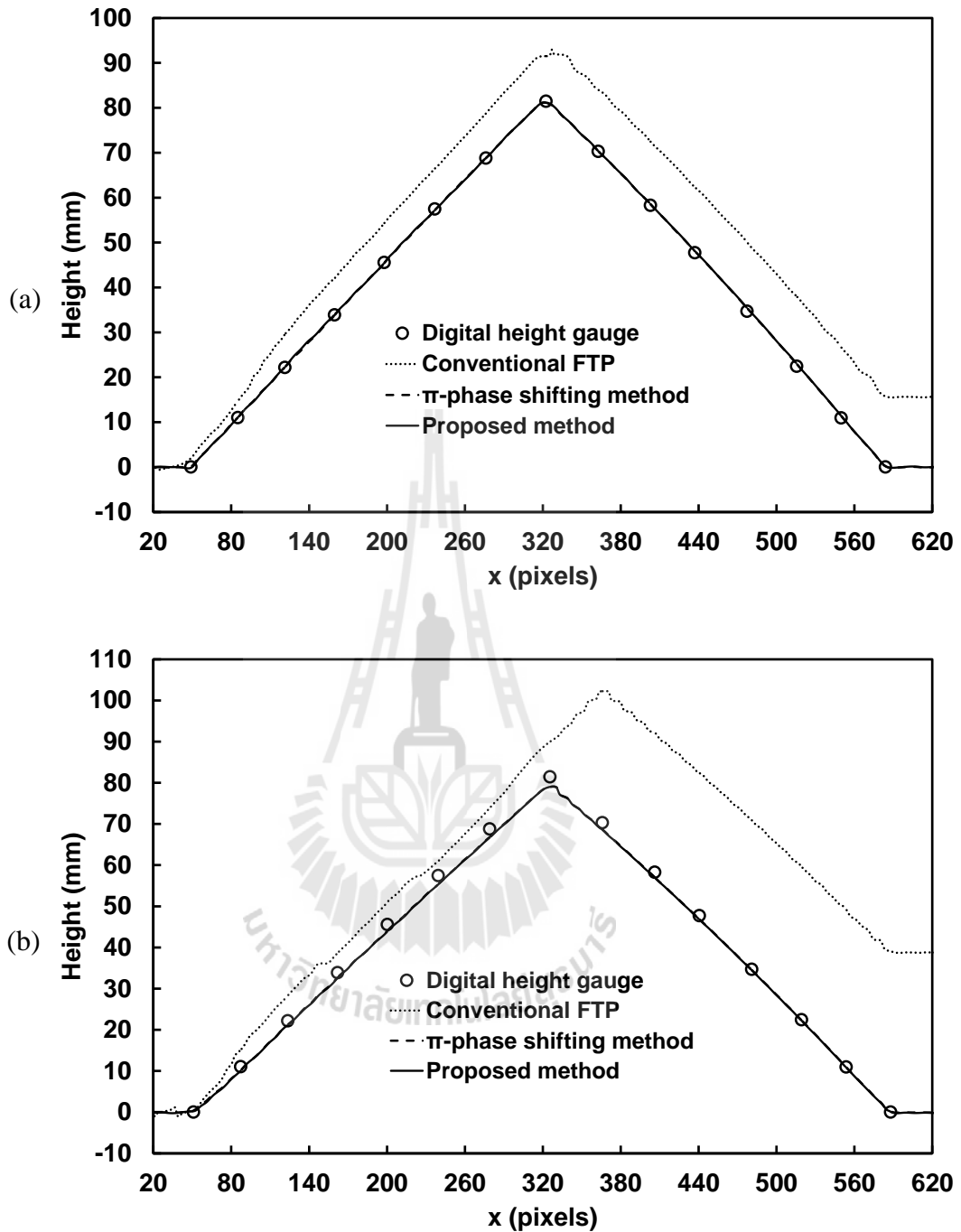


**Figure 4.16** Height profiles of the isosceles prism with the slope of 1.22 reconstructed at the angle  $\theta = 28^\circ$  by using the conventional, the  $\pi$ -phase shifting and the proposed FTPs compared with the digital height gauge in situation that the gratings have the pitch of (a) 4.84 mm and (b) 3.24 mm, respectively.

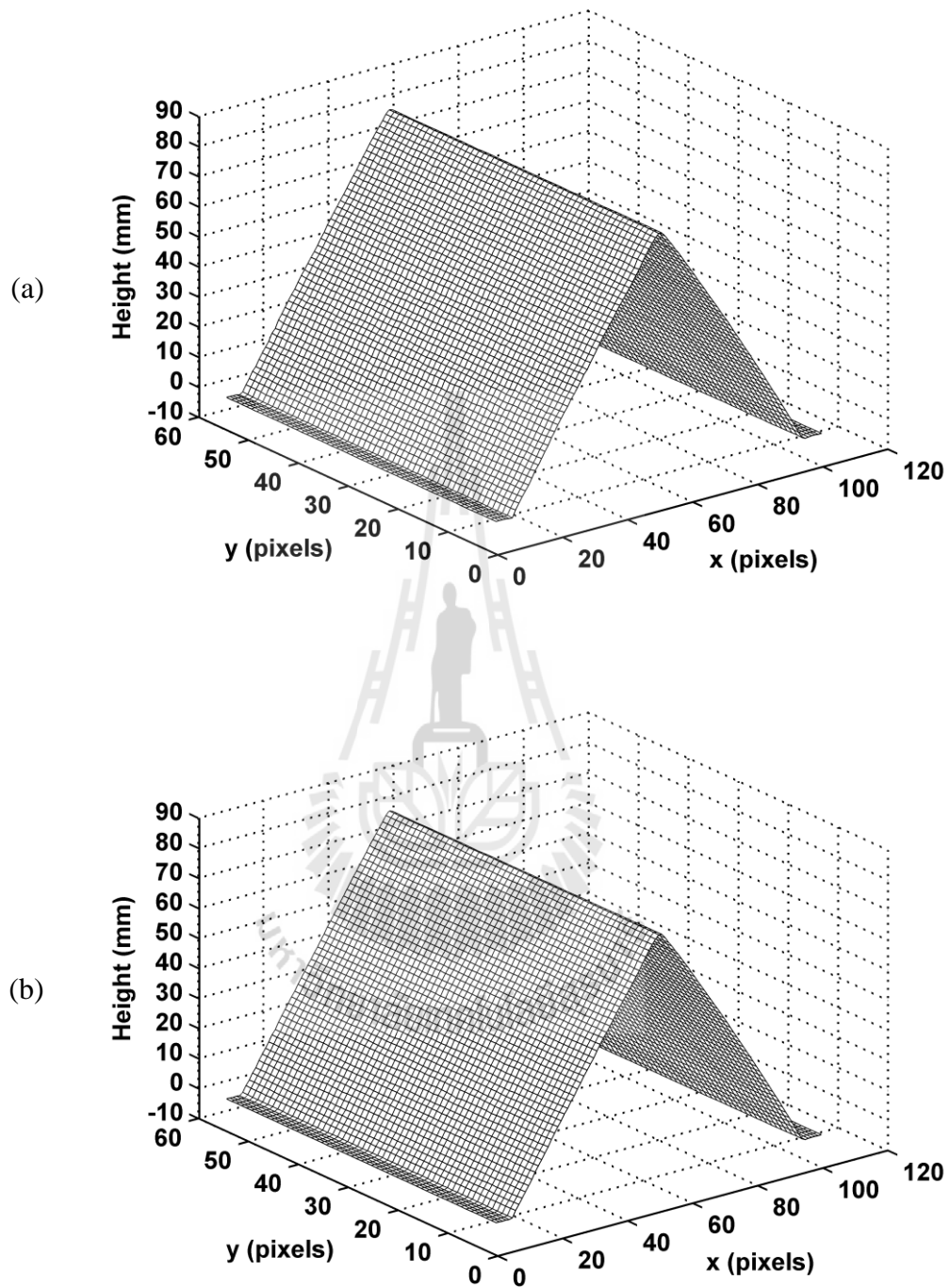


**Figure 4.17** 3-D height profile of the isosceles prism reconstructed in situation that the projected grating has the pitch of 4.84 mm at the angle  $\theta = 28^\circ$  by using (a) the  $\pi$ -phase shifting and (b) the proposed methods, respectively.

#### 4.4.3 Arbitrary-Shaped Bottle

To further verify feasibility of the proposed method, the surface profile of the plastic water bottle was reconstructed. Figures 4.18(a) and (b) show the deformed pattern of the bottle which was generated by projecting the grating with the pitch of 3.24 mm projected at the angle  $\theta = 8^\circ$  and  $12^\circ$ , respectively. Comparison of the two deformed grating patterns show that when the projection angle is  $12^\circ$ , there is shadow of the surface height appears along the left side of the bottle.

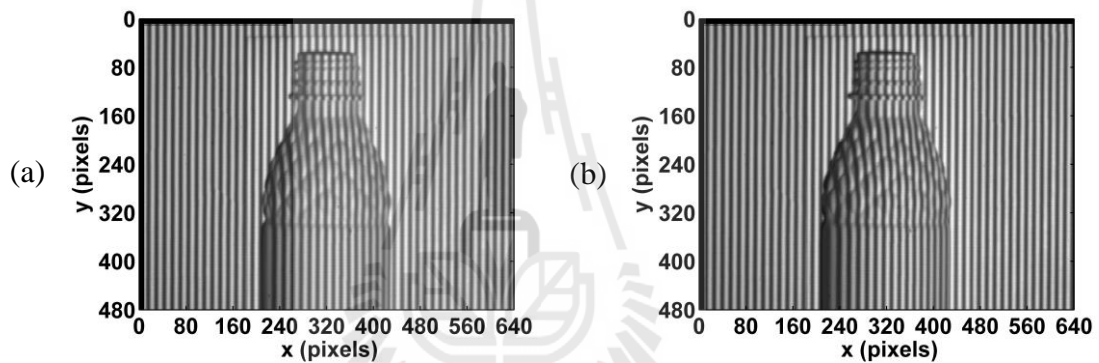


**Figure 4.18** Images of the grating patterns deformed by the plastic water bottle object in situation that the projected grating has the pitch of 3.24 mm at the angle  $\theta$  of (a)  $8^\circ$  and (b)  $12^\circ$ , respectively.

The intensities scanned at the 131<sup>th</sup> and 270<sup>th</sup> rows of the corresponding grating images shown in Figures 4.18(a) and (b) are presented in Figures 4.19(a), (b), (c) and (d), respectively. The 131<sup>th</sup> row corresponds to the neck support ring of the bottle, while the 270<sup>th</sup> row is associated with the bottle shoulder. Therefore, they have different surface profile and height. Since the shoulder area consists of multi-curved elements, Figures 4.19(c) and (d) show more rapid intensity change than the

others. Furthermore, due to the shadow, discontinuities appear on the left side of the signal deformed by the object.

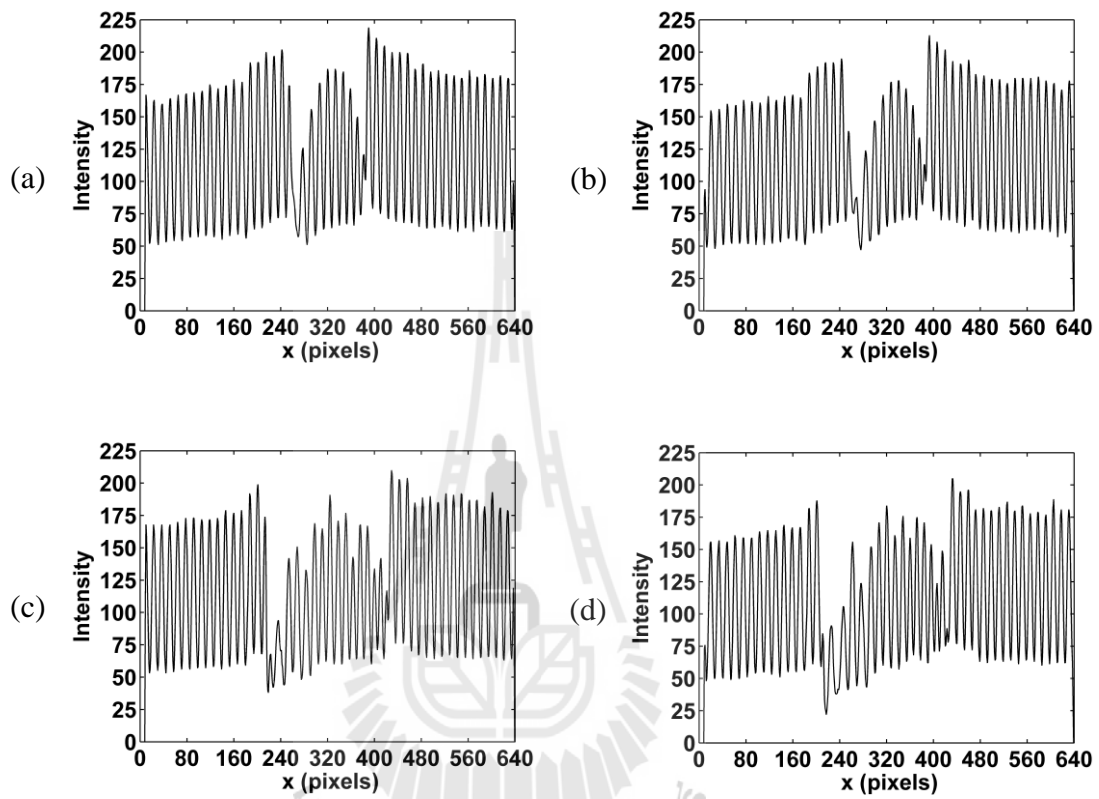


**Figure 4.19** Intensities scanned at the 131<sup>th</sup> row of (a) Figure 4.18(a) and (b) Figure 4.18(b). Intensities scanned at the 270<sup>th</sup> row of (c) Figure 4.18(a) and (d) Figure 4.18(b), respectively.

The resultant background elimination from the signals shown in Figures 4.19(a), (b), (c) and (d) are depicted in Figures 4.20(a), (b), (c) and (d), respectively. Due to the elimination of the background signal, the deformed gratings have almost symmetric positive and negative intensities. However, the signal discontinuity still exists.

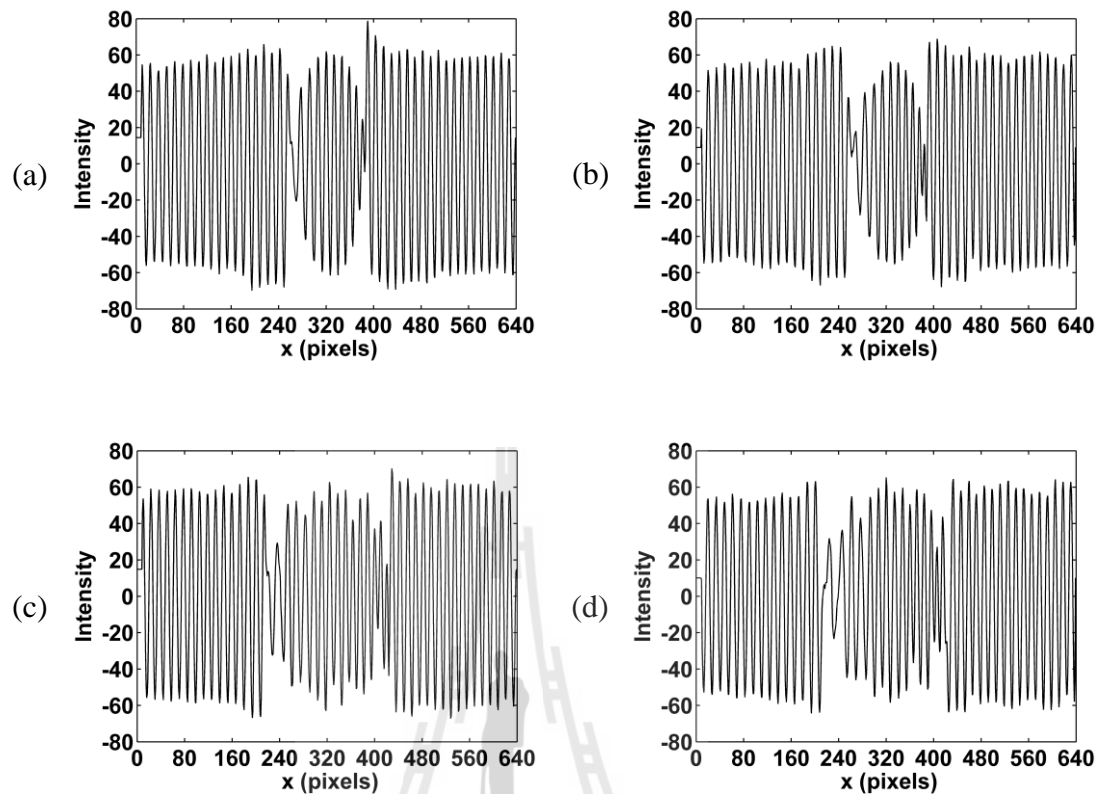


**Figure 4.20** Intensities scanned at the 131<sup>th</sup> row of the background eliminated grating patterns obtained from (a) Figure 4.19(a), (b) Figure 4.19(b). Intensities scanned at the 270<sup>th</sup> row of the background eliminated grating patterns obtained from (c) Figure 4.19(c) and (d) Figure 4.19(d), respectively.

The power spectra of the background eliminated grating patterns in Figures 4.20(a), (b), (c) and (d) are shown in Figures 4.21(a), (b), (c) and (d), respectively. It is obvious from this figure that the first-order spectra can be easily identified. Due to the bigger angle of  $12^\circ$ , both the first-order spectra shown in Figures 4.21(c) and (d) obtained from the intensities scanned at the 270<sup>th</sup> row have

broader spatial frequency components than Figures 4.21(a) and (b) which are obtained from the intensities scanned at the 131<sup>st</sup> row.

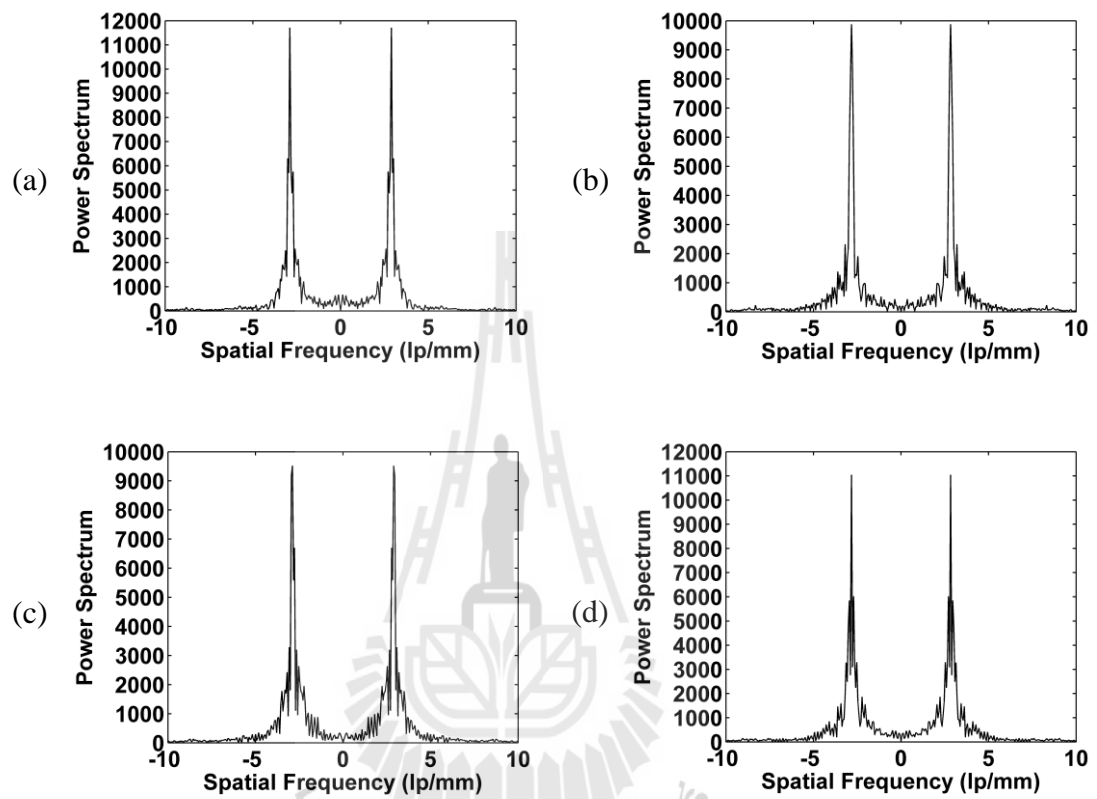


**Figure 4.21** Power spectra of the background eliminated grating patterns obtained from (a) Figure 4.20(a), (b) Figure 4.20(b), (c) Figure 4.20(c), (d) Figure 4.20(d), (e) Figure 4.20(e) and (f) Figure 4.20(f), respectively.

Figures 4.22(a) and (b) show plots of the height profile of the neck support ring reconstructed by using the conventional, the modified and the proposed FTPs at the angle  $\theta = 8^\circ$  and  $12^\circ$ . The height profiles reconstructed by the modified and the proposed methods at the angle  $\theta = 8^\circ$  are in good agreement with the measurements by the digital height gauge. In contrast, the conventional FTP fails to

reconstruct the profile, because of the overlapping of the first-order and the zeroth-order spectra. Unlike the smaller angle  $\theta = 8^\circ$ , the heights reconstructed on the left and the right sides by all FTP methods at the angle  $\theta = 12^\circ$  are incorrect. This may be caused by occurrence of the shadow which causes wrong phase modulation.

The height profiles of the bottle shoulder reconstructed at the angle  $\theta = 8^\circ$  and  $12^\circ$  are plotted in Figures 4.23(a) and (b), respectively. The modified and the proposed FTPs can reconstruct correctly the bottle profile only at the angle  $\theta = 8^\circ$ . Due to the shadow, all methods give the wrong reconstruction.



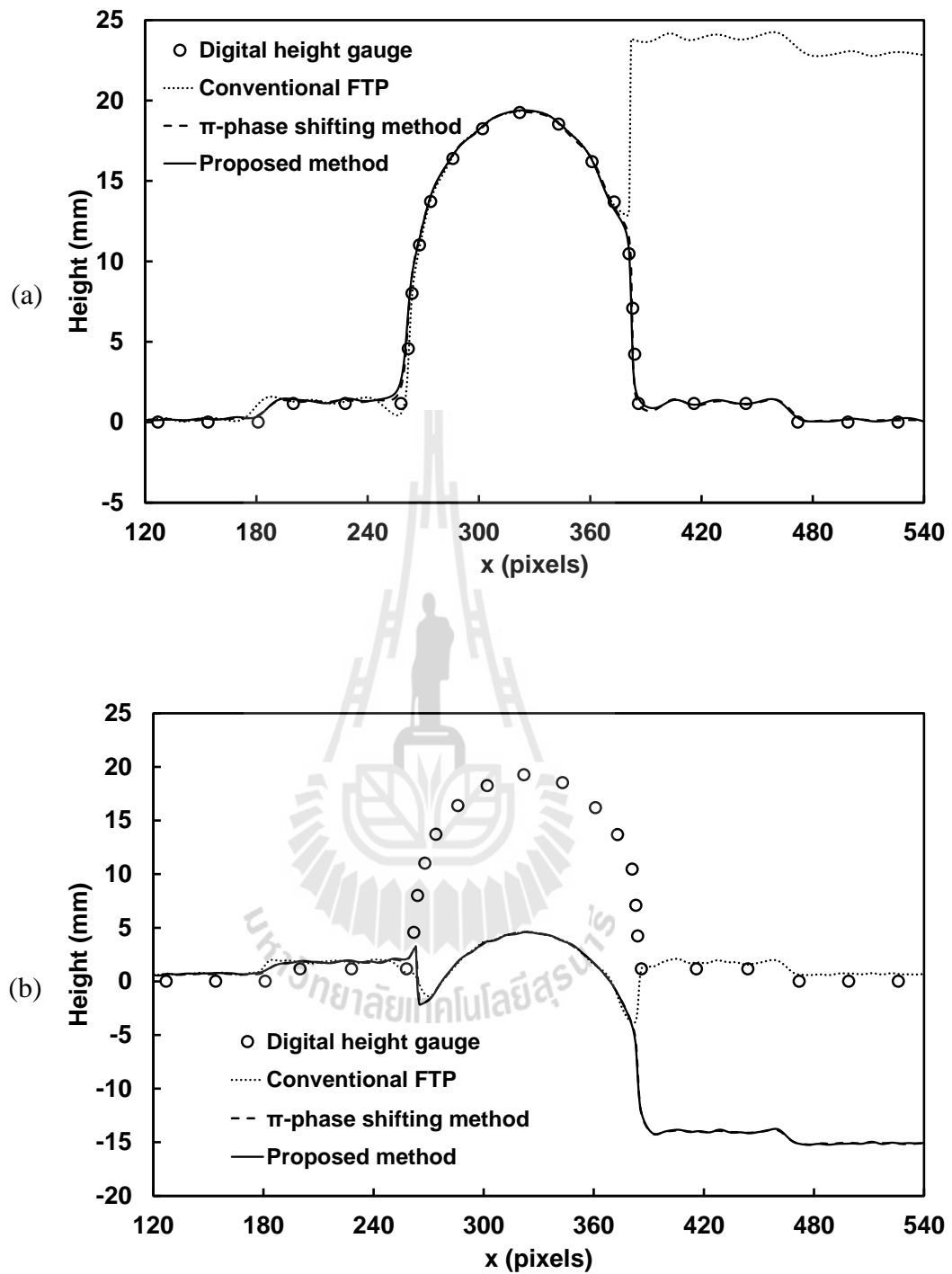


**Figure 4.22** Height profiles of neck support ring reconstructed by using the conventional, the  $\pi$ -phase shifting and the proposed FTPs compared with the digital height gauge in situation that the angle  $\theta$  is (a)  $8^\circ$  and (b)  $12^\circ$ , respectively.

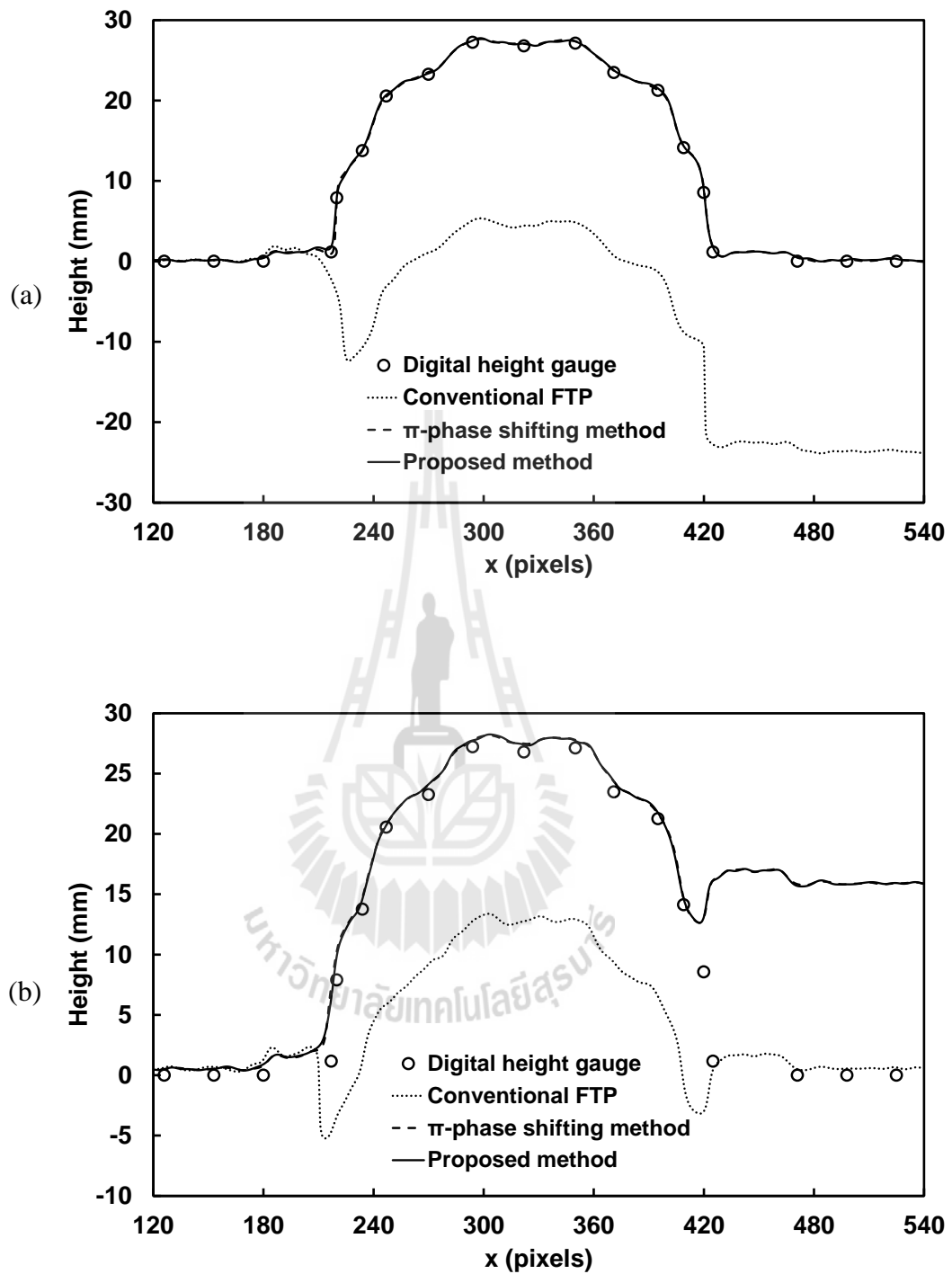


**Figure 4.23** Height profiles of the bottle shoulder reconstructed by using the conventional, the  $\pi$ -phase shifting and the proposed FTPs compared with the digital height gauge in situation that the angle  $\theta$  is (a)  $8^\circ$  and (b)  $12^\circ$ , respectively.

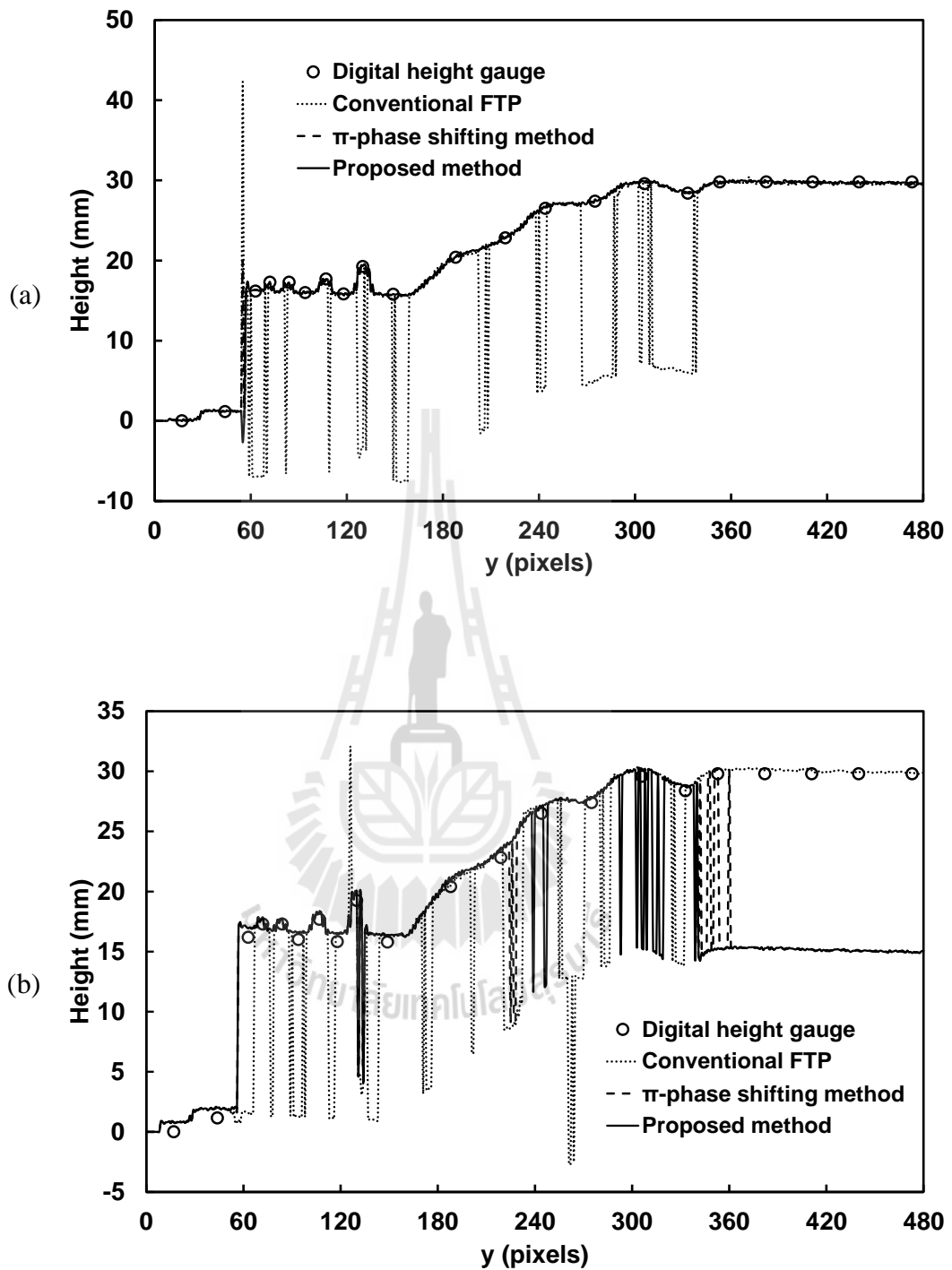


**Figure 4.24** Height profiles along the vertical direction of the bottle reconstructed by using the conventional, the  $\pi$ -phase shifting and the proposed FTPs compared with the digital height gauge in situation that the angle  $\theta$  is (a)  $8^\circ$  and (b)  $12^\circ$ , respectively.

Figures 4.24(a) and (b) show the height profiles reconstructed at the 323<sup>rd</sup> column along the  $y$  axis at the angle  $\theta = 8^\circ$  and  $12^\circ$  respectively. The height reconstructions at the angle  $\theta = 8^\circ$  shown in Figure 4.24(a) verify the usefulness of the  $\pi$ -phase shifting and the background elimination methods. However at bigger angle  $\theta = 12^\circ$ , it is difficult to reconstruct correctly the height profile, regardless of the methods. This is mainly caused by the occurrence of the shadow on the left side.

The 3-D height profile reconstructed at the angle  $\theta = 8^\circ$  by using the  $\pi$ -phase shifting and the background elimination methods are shown in Figures 4.25(a) and (b), respectively. The reconstructions are done by using three different filters because the bottle has complex shape. The first filter has bandwidth of 1.325~6.506 lp/mm, the second one is 1.386~6.506 lp/mm, while the third one is 1.687~6.325 lp/mm. It is clear that the height profiles reconstructed by using the  $\pi$ -phase shifting and the proposed methods are very similar. Thus, the proposed FTP has advantages over the  $\pi$ -phase shifting method in that it requires less number of grating projection.

Figures 4.26(a) and (b) show the reconstructions at the angle  $\theta = 12^\circ$  by using the  $\pi$ -phase shifting and the background elimination methods, respectively. Although several filters are used to reconstruct the 3-D profile, the effect of the shadow on the phase modulation is very severe. As a result, the  $\pi$ -phase shifting and the proposed methods cannot reconstruct the correct profile.

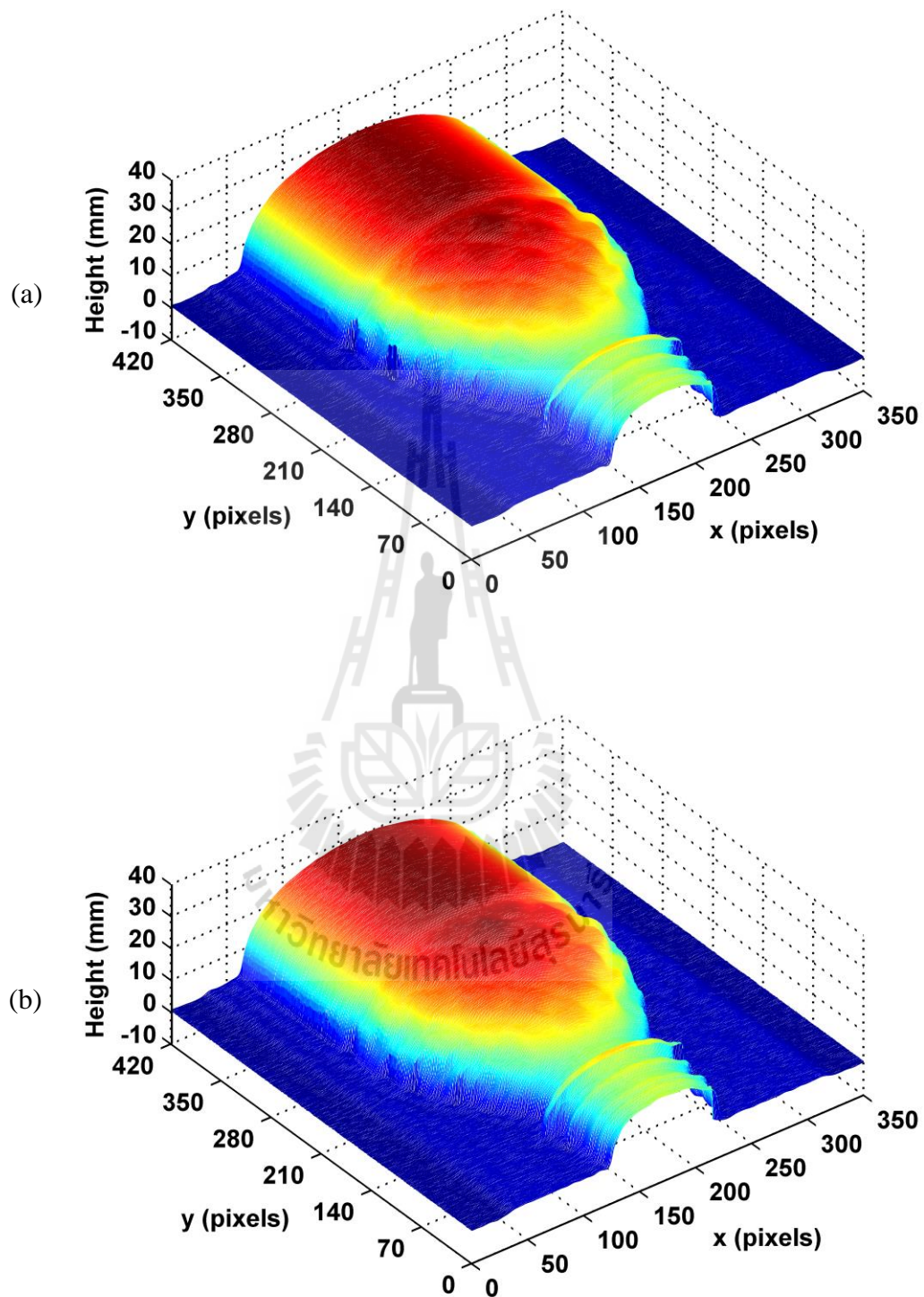


**Figure 4.25** 3-D height profiles of the bottle reconstructed at the angle  $\theta = 8^\circ$  by using (a) the  $\pi$ -phase shifting and (b) the proposed method, respectively.

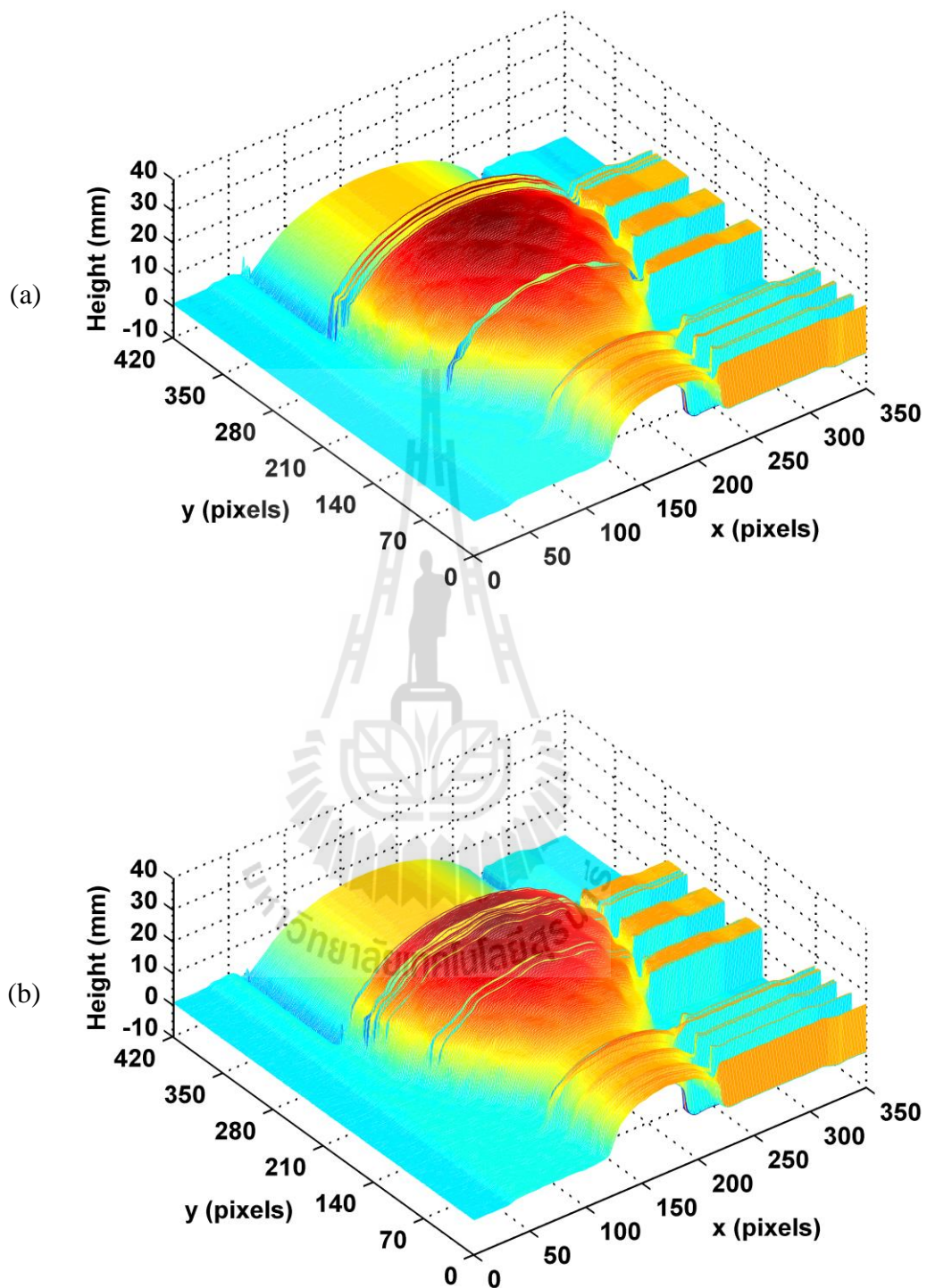


**Figure 4.26** 3-D height profiles of the bottle reconstructed at the angle  $\theta = 12^\circ$  by using (a) the  $\pi$ -phase shifting and (b) the proposed method, respectively.

# CHAPTER V

## CONCLUSIONS

### 5.1 Conclusions

A new method for improving the FTP performance by using non  $\pi$ -phase shifting background elimination method has been proposed and experimentally verified. By eliminating the non-uniform background signal, the proposed FTP can reconstruct object profile with different slopes. The proposed FTP is implemented by using the images of the object being studied and the reference plane. Firstly, the mean intensity is removed from each image. Secondly, the resultant object image scaled by its contrast is then subtracted from the grating image deformed by the object. This process is also performed for the images corresponding to the reference plane. This removes totally the background signal.

The feasibility of the proposed method has been verified by using the isosceles prism with different slopes and the 600 ml water bottle as the test objects. The experimental results presented in Chapter 4 show that

- Although the proposed method employs the same number of grating patterns as the conventional FTP, the measurement performance is as good as that obtained by using the  $\pi$ -phase shifting method. Consequently, it suffers less from the phase error caused by the jitter of the projected grating.

- The grating pattern with narrow pitch cannot be used for the reconstruction of the object profile having sharp discontinuity, because its deformed grating image may not be resolved by the camera system, yielding wrong height.
- The bigger the projection angle, the smoother the reconstructed profile. This is because the bigger angle encodes broader spatial frequency components.
- Wrong height reconstruction may also be produced when the deformed grating image is corrupted by shadow of the object profile. Therefore, the shadow becomes the limiting factor of the angle.
- When the object has complex profile, multiple filters are required to reconstruct different parts of the object.

## 5.2 Future Work

In this research, the proposed FTP method has been verified by using large objects. However, the 3-D shape reconstruction of small objects is practically more difficult. For example, in printed circuit board manufacturing process, shape and amount of solder paste which create joints between pads and component leads affects quality of the joints. Due to minimum grating pattern requirement, our proposed method can be used for the reconstruction of the solder paste in real-time manufacturing inspection. Design and implementation of the proposed FTP will be investigated for further research.



## **REFERENCES**

## REFERENCES

- Fukaishi, M., Nakamura, K., Heiuchi, H., Hirota, Y., Nakazawa, Y., Ikeno, H., Hayama, H., and Yotsuyanagi, M. (2000). A 20-Gb/s CMOS multichannel transmitter and receiver chip set for ultra-high-resolution digital displays. **IEEE Journal of Solid-State Circuits**. 35(11): 1611-1618.
- Geng, J. (2011). Structured-light 3D surface imaging: A tutorial. **Advances in Optics Photonics**. 3: 128-160.
- Gorthi, S.S. and Rastogi, P. (2010). Fringe projection techniques: Whither we are. **Optics and Laser in Engineering**. 48(2): 133-140.
- Hsiao, K-J and Lee, T-C. (2008). The Design and Analysis of a Fully Integrated Multiplying DLL With Adaptive Current Tuning. **IEEE Journal of Solid-State Circuits**. 43(6): 427-1435.
- Li, J., Su, X.Y., and Guo, L.R. (1990). Improved Fourier-transform profilometry for automatic measurement of three-dimension object shapes. **Optics and Laser in Engineering**. 29(12): 1439-1444.
- Martinez, A., Rayas, J.A., Cordero, R.R., Balieiro, D., and Labbe, F. (2012). Leaf cuticle topography retrieved by using fringe projection. **Optics and Laser in Engineering**. 50: 231-235.
- Meneses, J., Gharbi, T., and Cornu, J.Y. (2002) Three-dimensional optical high-resolution profiler with a large observation field: foot arch behavior under low static charge studies. **Applied Optics**. 41(25): 5267-5274.

- Pavlovych, A. and Stuerzlinger, W. (2010). Effects of Latency Jitter and Dropouts in Pointing Tasks. In **Proceedings of the Graphics Interface 2010**. (pp. 30-32).
- Peli, E. (1990). Contrast in complex images. **Journal of the Optical Society of America**. 7(10). 2032-2040.
- Quan, C., He, X.Y., Wang, C.F., Tay, C.J., and Shang, H.M. (2001). Shape measurement of small objects using LCD fringe projection with phase shifting. **Optics Communications**. 189: 21-29.
- Sajan, M.R., Tay, C.J., Shang, H.M., and Asundi, A. (1997). Time delay and integration imaging for inspection and profilometry of moving object. **Optics and Laser in Engineering**. 36(9): 2573-2578.
- Spagnolo, G.S., Guattari, G., Sapia, C., Ambrosini, D., Paoletti, D., and Accardo. (2000). Contouring of artwork surface by fringe projection and FFT analysis. **Optics and Laser in Engineering**. 33: 141-156.
- Su, X. and Chen, W. (2004). Reliability-guided phase unwrapping algorithm: A review. **Optical and Laser in Engineering**. 42: 245-261.
- Su, X.Y., Zhou, W.S., von Bally, C., and Vukicevic, D. (1992). Automated phase-measuring profilometry using defocused projection of a Ronchi grating. **Optics Communications**. 94(6): 561-573.
- Takeda, M. and Mutoh, K. (1983). Fourier transform profilometry for the automatic measurement of 3-D object shapes. **Applied Optics**. 22(24): 3977-3982.
- Tavares, P.J. and Vaz, M.A. (2006). Orthogonal projection technique for resolution enhancement of the Fourier transform fringe analysis method. **Optics Communications**. 266: 465-468.
- Tay, C.J., Toh, S.L., and Shang, H.M. (1998). Time delay and integration imaging for

internal profile inspection. **Optics and Laser Technology**. 30: 459-465.

- Yamaguchi, K., Hori, Y., Nakajima, K., Suzuki, K., Mizuno, M., and Hayama, H. (2009). A 2.0 Gb/s Clock-Embedded Interface for Full-HD 10-Bit 120 Hz LCD Drivers With 1/5-Rate Noise-Tolerant Phase and Frequency Recovery. **IEEE Journal of Solid-State Circuits**. 44(12): 3560-3567.
- Yi, J. and Huang, S. (1997). Modified Fourier-transform Profilometry for the measurement of 3-D steep shapes. **Optical and Laser in Engineering**. 27: 493-505.
- Zhang, Q. and Su, X. (2005). High-speed optical measurement for the drumhead vibration. **Optics Express**. 13(8): 3110-3116.
- Zhou, W.S. and Su, X.Y. (1994). A Direct Mapping Algorithm for Phase-measuring Profilometry. **Journal of Modern Optics**. 41: 89-94.

# CURRICULUM VITAE

**Name** Mr. Jaron Wongjarern  
**Nationality** Thai  
**Born** June 27, 1985  
**Address** House No. 78, Village No. 10, Phra Khru sub-district, Mueang district,  
Buri Ram province, 31000, Thailand  
**E-mail** jaron.wongjarern@gmail.com

## Education Background

- Diploma of Electronics (Industrial Electronics)  
Technology Laemchabang College, Chonburi  
May 20, 2004 – May 1, 2006
- Bachelor of Engineering in Electronics and Telecommunication  
Rajamangala University of Technology Isan, Nakhon Ratchasima  
June 4, 2007 – October 10, 2010

## Publications

- Wongjarern, J, et al. (2014). Fourier transform profilometry by using digital dc subtraction. In **Proceedings of SPIE-The International Society for Optical Engineering**. vol. 9234. (pp. 923412).

## Grants and Fellowships:

- SUT outstanding academic performance scholarship for 2011-2012.